IMPROVED CHARACTERIZATION OF WHITE MATTER FIBER BUNDLES USING

DIFFUSION MRI

By

Xin Hong

Thesis

Submitted to the Faculty of the

Graduate School of Vanderbilt University

in partial fulfillment of the requirements

for the degree of

MASTER OF SCIENCE

in

Biomedical Engineering

December, 2006

Nashville, Tennessee

Approved:

Professor Adam W. Anderson

Professor Mark D. Does

To my beloved parents

ACKNOWLEDGEMENTS

I would like to thank Dr. Adam Anderson for his guidance, patience, and support for this project. I would like to thank Dr. Mark Does for his helpful advice. I would also like to thank Dr. Zhaohua Ding for his help with the smoothing process.

Finally, I would like to thank my husband, Jian, for his love, encouragement and support.

TABLE OF CONTENTS

Page

Chapter

LIST OF TABLES

LIST OF FIGURES

LIST OF ABBREVIATIONS

ACC — Angular Correlation Coefficient

ADC — Apparent Diffusion Coefficient

atr — anterior thalamic radiation

cc — corpus callosum

cg — cingulum bundle

cpt — corticopontine tract

cst — corticospinal tract

D — Diffusion Coefficient, Diffusivity

DSI — Diffusion Spectrum Imaging

DTI — Diffusion Tensor Imaging

FA — Fractional Anisotropy

FAD — Fiber Angular Distribution

FORECAST — Fiber ORientation Estimated using Continuous Axially Symmetric Tensors

HARD — High Angular Resolution Diffusion

HARDI — High Angular Resolution Diffusion Imaging

MRI — Magnetic Resonance Imaging

ODF — Orientation Distribution Function

PAS — Persistent Angular Structure

PGSE — Pulsed Gradient Spin Echo

QBI — Q-Ball Imaging

RF	Radio Frequency
ROI	Region Of Interest
RSS	Residual Sum of Squares
sfo	superior fronto-occipital fasciculus
SH	Spherical Harmonic
slf	superior longitudinal fasciculus
SNR	Signal to Noise Ratio
vtc	ventricle

LIST OF SYMBOLS

$Y_{lm}(\theta, \varphi)$ Spherical harmonic of order l and degree of phase factor m

l Order of spherical harmonic

m Degree of phase factor

$\lambda_\perp$ Perpendicular diffusivity

S_0 Diffusion un-weighted signal

S Diffusion weighted signal

$\widetilde{b}$ Diffusion weighting matrix

$tr(\widetilde{b})$ Trace of the diffusion weighting matrix

b Trace of the diffusion weighting matrix

F Complex function defined on the unit sphere

f_{lm} SH expansion coefficients of F

L Maximum order of SH expansion

$\vec{S}$ Vector of the diffusion weighted signal

$\vec{s}_{lm}$ Vector of the expansion coefficients of $\vec{S}$

$\widetilde{X}$ Design matrix

$nDirs$ Number of diffusion weighted measurements

$nTerms$ Total number of terms of the SHs

θ Ppolar angle of the spherical coordinates

φ Azimuthal angle of the spherical coordinates

k Convolution kernel

c_l	Convolution kernel expansion coefficients
A_l	l^{th}-order coefficients of the Legendre polynomial expansion of function $e^{-tr(\tilde{b})\left(\lambda_{\parallel}-\lambda_{\perp}\right)x^2}$
$\vec{p}_{lm}$	Vector of the expansion coefficients of FAD
$P(\theta,\varphi)$	Fiber angular distribution at angle (θ,φ)
$\widetilde{R}$	Constraint matrix
ω	Weighting factor in regularization
$\widetilde{A}_l$	Matrix that maps $\vec{p}_{lm}$ to $\vec{S}$
$\sigma^2_{s_0}$	Variance of the diffusion un-weighted signal
σ^2_s	Variance of the diffusion-weighted signal

CHAPTER I

INTRODUCTION

Overview

Diffusion Tensor Imaging (DTI) (1) has become the primary imaging modality for non-invasive characterization of the micro structure of living tissues, particularly of human white matter. The technique is based on the fact that the self-diffusion of the water molecules is sensitive to the microscopic composition, structure, and organization of the tissues (2,3). Despite its success in research areas such as neural fiber tractography (4-6) and in various clinical applications (7-21), the technique suffers from some fundamental limitations (22). One major problem is that the classic tensor model is not able to adequately describe non-Gaussian diffusion, and thus not able to provide reliable estimations of the underlying tissue properties. New imaging techniques such as High Angular Resolution Diffusion Imaging (HARD, or HARDI) (23-27) and new data reconstruction methods such as the Fiber ORientation Estimated using Continuous Axially Symmetric Tensors (FORECAST) model (28) have been proposed to address the problem. Based on the multiple-tensor model and HARD data, FORECAST is able to provide a more accurate description of diffusion properties, especially in complex areas where the classic tensor model fails. The overall goal of this study is to develop new

techniques to improve the FORECAST analysis and obtain more reliable estimations of the tissue properties.

This chapter includes: (a) the basic concept of diffusion and the properties of diffusion that are measured and analyzed in this study, (b) the principles of Diffusion Tensor Imaging, its applications and limitations, (c) new diffusion MRI techniques including the FORECAST model, and (d) a summary of the goals of this study.

Diffusion and its Properties

The phenomenon of diffusion, also called Brownian motion, refers to the random translational motion of water molecules driven by thermal energy. There are two important aspects in describing diffusion. In a homogeneous medium where water molecules can move freely, the amount of movements is described statistically by the Diffusion Coefficient, or diffusivity, D, a scalar measure equal to the mean squared molecular displacement per unit time. Diffusivity relies on several intrinsic properties of the medium: the mass of the molecules, the temperature, and the viscosity. On the other hand, in heterogeneous media, such as a biological sample, the measured diffusivity in an imaging voxel is the ensemble average of all the water molecules within the voxel, which is usually different from the intrinsic diffusion coefficient measured from a homogeneous medium. To distinguish these two concepts, the averaged diffusivity is named the Apparent Diffusion Coefficient (ADC). ADC depends not only on the media's intrinsic

properties, but also on the measurement parameters, such as the voxel size.

In addition to the amount of the displacement, water diffusion has another important property, its directionality. If the averaged displacements are identical in all directions within a given elapsed time, the diffusion is isotropic. Otherwise, the diffusion is anisotropic if the displacements are different along different directions. One example of isotropic diffusion occurs in the cerebrospinal fluid in the brain ventricle, where water molecules can move freely in any direction within the typical measurement time. In tissues like neural fibers, where the cellular architecture is highly organized, water encounters fewer barriers (such as membranes or myelin) along the primary axis of the fibers than perpendicular to this axis. Therefore, the molecular displacement along the fiber orientation is significantly larger than in other directions, showing strong anisotropy (29,30).

The two properties of the water diffusion, the overall diffusivity and its directional dependence, can provide useful information about the microscopic structure of the biological tissues. Given a proper diffusion time (typically 30~50 ms for human brain diffusion MRI), the random walk of the water molecules may reflect the restrictions and hindrances by various barriers, such as macromolecules and cellular membranes, resulting in different diffusivity properties from the freely diffusing bulk water. The microstructure of the samples can thus be inferred based on the measured diffusivity. In brain white matter, the degree of diffusion anisotropy is mainly determined by the packed and coherent axonal membranes, with some influence from myelin and other intracellular

3

micro structures as well (3). Therefore, diffusion anisotropy provides a unique way to non-invasively probe the neural fibers' structure and topological organization.

Diffusion Tensor Imaging

Diffusion properties are usually measured with a Pulsed Gradient Spin Echo (PGSE) pulse sequence in MRI experiments (31,32), featuring a pair of identical diffusion sensitizing gradient pulses applied along a prescribed direction before and after the 180º refocusing RF pulse. Due to the first gradient pulse, molecules at different positions will precess at different frequencies and thus will accumulate phase angles that depend on the molecules' positions along the gradient direction. The 180º RF pulse and the second gradient pulse aim to cancel the position dependent phase angle. The spins that are de-phased by the first pulse will re-phase if they remain stationary during the time between the two gradients. Otherwise, if the water molecules diffuse to different positions, the effect of the first gradient can not be completely reversed by the second one. The de-phased spins will thus result in an attenuated signal intensity compared to the intensity measured without diffusion weighting:

$$S = S_0 e^{-tr(\widetilde{b})D} \qquad [1]$$

where S and S_0 are the signal intensity measured with and without the diffusion sensitizing gradients (also known as the diffusion weighted signal and un-weighted signal), respectively. $\widetilde{b}$ is the diffusion weighting matrix describing the strength and

timing of the diffusion gradients. With negligible gradient ramp times and gradient cross

terms, the diffusion sensitivity of the gradients can be represented by the trace of the

matrix $\widetilde{b}$, $tr(\widetilde{b})$, also known as the diffusion weighting factor, or simply the b factor.

According to Eq. [1], the diffusion coefficient D can be calculated with as few as two

measurements, one with the diffusion sensitizing gradients, and the other without the

gradients.

For isotropic diffusion, the measured ADCs are identical when the diffusion

gradients are applied in different directions. For anisotropic diffusion, the greater the

diffusion along a certain direction, the more attenuated the measured signal will be along

that direction, i.e., the measured ADC depends on the direction of the applied gradients.

Therefore, the scalar ADC is not sufficient to fully describe anisotropic diffusion in 3D

space. In the early 1990s, the tensor model was proposed to better address this problem

(1). Instead of a scalar ADC, the diffusion tensor, a positive definite, symmetric

3×3 matrix with six independent elements is utilized to characterize anisotropic diffusion.

To measure the diffusion tensor, at least seven independent measurements are required,

six diffusion weighted measurements along six non collinear directions, plus one

un-weighted. If the diffusion gradients are aligned with the sample's natural symmetry

axes (also called the principal axes), the resulting tensor is a diagonal matrix, with

diagonal elements corresponding to the ADCs along these axes. In most of the

experiments on living samples, the tissues' principal axes are unknown, it is thus

impossible to align the diffusion gradients with them. In this case, the eigenvalues of

tensor indicate the ADCs along the three principal directions given by the corresponding eigenvectors.

The diffusion tensor provides three kinds of information about the tissue's properties. First, the trace of the tensor describes the overall diffusivity (mean over all directions) within the imaging voxel. This measure is related to properties such as the cell density, and the volume ratio of intracellular and extracellular space. Second, diffusion anisotropy can be described by various anisotropy indices derived from the tensor. These indices describe how much the diffusion profile deviates from isotropy. Useful information about the tissue's microstructure such as degree of myelination of the neural fibers can be inferred from these indices. One of the most widely used anisotropy indices is Fractional Anisotropy (FA), which can be calculated from the eigenvalues of the tensor, ranging from 0 for isotropic diffusion to 1 for anisotropic diffusion. Third, the eigenvector associated with the largest eigenvalue of the diffusion tensor is assumed to indicate the principal orientation of the underlying structure. Many algorithms have been developed to map neural fiber tracts and study the connectivity between different regions of the brain based on this information (33,34).

Due to the ability of DTI to probe the microstructure of tissues non-invasively, it has been applied to a wide range of research areas such as the brain development, maturation (7), and aging (13), and many clinical applications to disease and injury detection, including acute stroke (8,14,15), multiple sclerosis (9,16-18), epilepsy (10,19) and brain tumor (12,20,21), and treatment evaluation (35,36) (for a review of the clinical

application, see (37)).

Although the diffusion tensor model works fairly well in identifying fiber orientations in some parts of the brain, it fails in other regions. One of the most significant limitations of DTI is its inability to describe diffusion where orientation heterogeneity occurs within one image voxel (22,38).

One reason for this problem is the size mismatch between the imaging voxel and the underlying structures. The typical neural axon diameter ranges from less than 1 micron to more than 30 microns in human brain(39), while the typical voxel size in the clinical and research environment is on the scale of millimeters. Therefore, it is inevitable that some of the voxels contain fibers of heterogeneous diffusion properties. Several different situations may occur. First, multiple fiber populations of different orientations may show up within one voxel, for example, the so-called fiber crossing, fiber kissing, and fiber joining. Second, fiber populations of the same orientation but different intrinsic diffusion properties may occur, for example, when one of the fiber bundles is affected by some disease. Third, even a single fiber bundle may change its orientation within one voxel, which is referred to as fiber bending. Fourth, both intra-axonal and extra-axonal spaces with different diffusion properties may share a voxel. All these possibilities complicate the interpretation of the diffusion tensor. The conventional second-order tensor model is based on the single Gaussian diffusion assumption, which gives only one principal direction of the diffusion displacements, the tensor model is therefore insufficient in describing diffusion with multiple preferential directions.

7

This limitation results in two major problems of the tensor model in the areas where complicated structures are present. First, the principal eigenvector associated with the largest eigenvalue can no longer be assumed to be the dominant diffusion direction, which makes fiber tracking based on the tensor model unreliable. Second, the anisotropy indices derived from the tensor model may be misinterpreted when two fiber bundles with different anisotropy share a voxel (22,40).

High Angular Resolution Diffusion Imaging

To address DTI's problems and provide more accurate measurement of diffusion in the brain, people developed new imaging techniques, and new data reconstruction methods, as well.

One way to reveal more details of the diffusion process is to obtain measurements in more directions and with more levels of diffusion sensitivity (multiple b values). One example is Diffusion Spectrum Imaging (DSI) (41), which is based on the Fourier relationship between the diffusion propagator function and the measured signal (32). Though DSI is model independent and thus capable of resolving multiple intravoxel fiber populations, it suffers from two major problems, long image acquisition time and the requirement of strong field gradients. Both of these drawbacks limit its clinical applications.

To accommodate the usual requirements of the clinical environment: short imaging time and modest gradient strength, an alternate imaging method termed High Angular Resolution Diffusion Imaging was developed (23-27). Taking the middle ground between the DTI and DSI, HARD imaging obtains measurements in more than six directions with single b value, aiming to achieve a balance between detailed information and requirements for long imaging time and strong gradients.

To extract diffusion properties and reveal tissue structural information from the HARD signal, several different reconstruction schemes were developed, including the multiple tensor model (23), generalized tensor model (26,42), spherical harmonic decomposition of the ADC profile (24,43), spherical harmonics deconvolution (44), Persistent Angular Structure (PAS) (27), circular spectrum mapping (45), and Q-Ball Imaging (QBI) (46-48). Among them, QBI is particularly popular due to its simple sampling scheme and straightforward, model-independent reconstruction. Instead of sampling a 3D Cartesian grid in the Q-space as in the DSI method, this technique samples only a spherical shell. This new sampling scheme not only reduces the imaging acquisition time, but also lowers the demand on the gradients. Based on the Funk-Radon transformation, the fiber Orientation Distribution Function (ODF) along any direction α is estimated directly by integration of the diffusion weighted signal measured along directions perpendicular to α. Since the reconstruction of ODF takes no priori assumption about the distribution of the underlying diffusion process, QBI is able to reveal multiple fibers within a voxel.

Although these techniques mentioned above are capable of resolving intravoxel multiple fibers, none of them provides information about the intrinsic diffusion properties. In certain developmental or pathological conditions, the change of intrinsic diffusivity (for example, due to change in cell density, or damage to the myelin layers) could result in decreased FA values. Decrease of coherence in fiber orientation could also reduce the FA. None of these data analysis approaches is able to distinguish the possible causes.

The FORECAST model

Fiber ORientation Estimated using Continuous Axially Symmetric Tensors is a new HARD data reconstruction technique based on a multiple tensor model (28). It assumes that within a voxel, different fiber components have same proton density, same relaxation properties, and negligible exchange between the components within the given diffusion time. The model further assumes that the diffusion tensor for each fiber component is axially symmetric, with one larger eigenvalue and the other two equal and smaller. The measured signal is the sum of contributions from all the individual tensors. With a further assumption of uniform mean and perpendicular diffusivity within each voxel, the diffusion weighted signal can be expressed as a convolution of the Fiber Angular Distribution (FAD) function and the response function from an ideal single fiber. The single fiber response function depends on the *b* value, the mean and the perpendicular diffusivities, and the angle between the diffusion gradient direction and the fiber

orientation. By expressing the functions in terms of Spherical Harmonic (SH), the convolution relationship between the measured signal and the fiber angular distribution becomes a simple algebraic equation in terms of their spherical harmonics coefficients. Once the perpendicular diffusivity is estimated from the relation between the signals, the b value and the presumed mean diffusivity, the single fiber response function is obtained. The fiber angular distribution function can then be recovered. The peaks of the FAD function provide information about the underlying fiber components. The orientation of each peak estimates the primary orientation of the fiber, and the magnitude of each peak is assumed to be proportional to the volume fraction of the corresponding fiber. Details of the calculation steps will be discussed in the METHODS section.

The FORECAST model shows several advantages over the QBI method. First, at moderate b levels FORECAST can not only better recover multiple fibers within a voxel, it is also capable of resolving fiber topology ambiguities such as crossing, kissing, joining, bending (49). Second, by estimating both the perpendicular diffusivity and fiber angular distribution in each voxel, FORECAST is capable of distinguishing two different causes of decreased FA, fiber coherence change or fiber intrinsic diffusivity change. Third, by expressing functions in SHs, the FORECAST model is computationally efficient, involving only linear matrix calculation, avoiding integration or interpolation.

Goals of this study

The goal of this study is to explore the FORECAST model's performance, specifically its dependence on measurement and reconstruction parameters, and develop new techniques to enhance the FORECAST model's reproducibility, and to find out the optimal way to apply the FORECAST analysis to clinical applications.

CHAPTER II

METHODS

Monte Carlo simulation was used to test the FORECAST model's dependence on various

imaging parameters, such as the b value, SNR, number of the diffusion gradient

directions, and various analysis parameters. After generating the ideal HARD signal

using certain imaging parameters, random noise with zero mean and standard deviation

of S_0/SNR was added to the ideal signal (both the diffusion weighted and un-weighted).

FORECAST analysis was performed using various parameters. Several figures of merit

were then calculated and compared between each set of imaging and analysis parameters.

In this chapter, we first present the basic formulas of the FORECAST reconstruction,

then introduce several methods to improve the FORECAST analysis, outline the

simulation procedure, and finally explain the figures of merit used for the performance

evaluation.

Spherical Harmonics

Before discussing FORECAST model, we first discuss how to approximate functions by

spherical harmonics. Spherical harmonics $Y_{lm}(\theta, \varphi)$ are a set of orthonormal basis

functions on the unit sphere, satisfying the spherical harmonic differential equation

$$\left[\frac{1}{\sin\theta} \frac{\partial}{\partial\theta}\left(\sin\theta \frac{\partial}{\partial\theta}\right) + \frac{1}{\sin^2\theta} \frac{\partial^2}{\partial\varphi^2} + l(l+1)\right]F = 0 \qquad [2]$$

where the non-negative integer l denotes the SH order, and the integer m denotes the

degree or phase factor (for each l, m ranges from $-l$ to l) (50). A complex function F

defined on the unit sphere can be expressed as a weighted sum of the harmonics, with a

different coefficient for each order and degree:

$$F(\theta,\varphi) = \sum_{l=0}^{\infty} \sum_{m=-l}^{l} f_{lm} Y_{lm}(\theta,\varphi) \qquad [3]$$

where f_{lm} are the SH expansion coefficients satisfying

$$f_{lm} = \int_0^{2\pi} \int_0^{\pi} Y_{lm}^*(\theta,\varphi) F(\theta,\varphi) \sin\theta\, d\theta\, d\varphi \qquad [4]$$

The $Y_{lm}(\theta,\varphi)$ are symmetric about the origin for all even orders l, and asymmetric for

all odd orders. The high order SHs describe the high angular frequency components of

the function, the low order SHs correspond to the low frequency components. The zero[th]

order SH, with the shape of a sphere, is able to describe isotropic diffusion; 2nd order SH

is the minimum requirement for describing single fiber diffusion; 4th order SH is required

to resolve two fiber populations, and so on. In theory, the higher the order, the higher the

angular resolution (28). In practical calculations, the infinite sum in Eq. [3] is usually

truncated to a maximum order L. The choice of the maximum order depends on the

properties of the function to be estimated. If the function is relatively smooth, a low order

approximation will be sufficient. Otherwise, high orders will be needed, at the cost of

increased noise sensitivity and computation time.
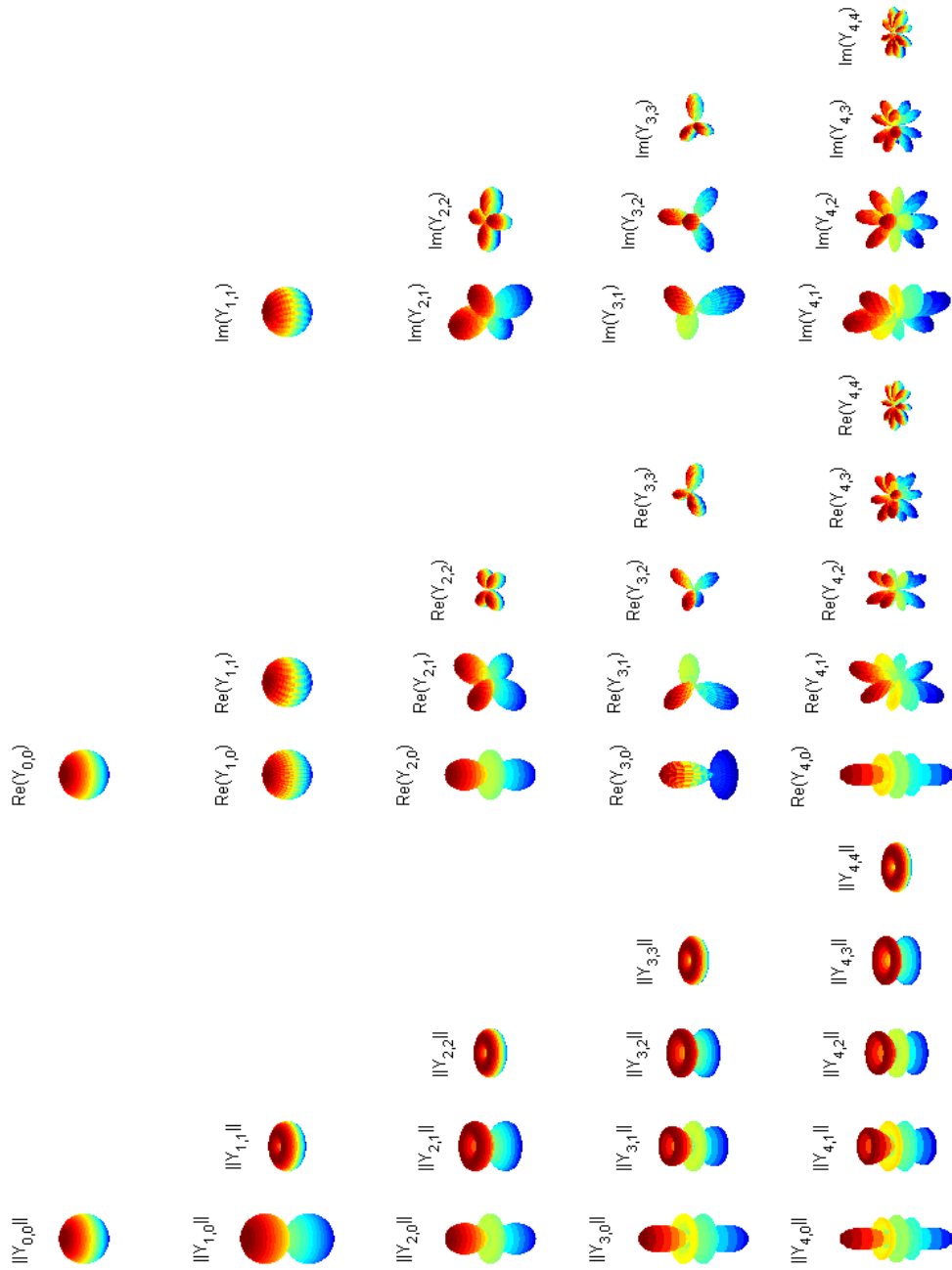
Figure 1. Plots of $\|Y_{lm}\|$, $\text{Re}(Y_{lm})$, and $\text{Im}(Y_{lm})$ up to 4th order

15

In this study, the diffusion weighted signals measured in various directions form a discrete function on a unit sphere, and thus can be approximated by a truncated series of SHs:

$$S = \sum_{l=0}^{L} \sum_{m=-l}^{l} s_{lm} Y_{lm} \qquad [5]$$

The relation expressed in the form of matrix multiplication is:

$$\vec{S} = \widetilde{X} \cdot \vec{s}_{lm} \qquad [6]$$

where $\vec{S}$ is a $nDirs \times 1$ vector of the diffusion weighted signal, $\vec{s}_{lm}$ the $nTerms \times 1$ SH expansion coefficients vector, and $\widetilde{X}$ the $nDirs \times nTerms$ design matrix consisted of spherical harmonics $Y_{lm}^{n} \equiv Y_{lm}(\theta_n, \varphi_n)$ of the nth diffusion direction in the nth row:

$$\widetilde{X} = \begin{pmatrix} Y_{0,0}^{1} & Y_{1,-1}^{1} & Y_{1,0}^{1} & Y_{1,1}^{1} & Y_{2,-2}^{1} & \cdots & Y_{L,L-1}^{1} & Y_{L,L}^{1} \\ Y_{0,0}^{2} & Y_{1,-1}^{2} & Y_{1,0}^{2} & Y_{1,1}^{2} & Y_{2,-2}^{2} & \cdots & Y_{L,L-1}^{2} & Y_{L,L}^{2} \\ \cdots & \cdots & & \cdots & \cdots & \cdots & \cdots & \cdots \\ Y_{0,0}^{nDirs} & Y_{1,-1}^{nDirs} & Y_{1,0}^{nDirs} & Y_{1,1}^{nDirs} & Y_{2,-2}^{nDirs} & \cdots & Y_{L,L-1}^{nDirs} & Y_{L,L}^{nDirs} \end{pmatrix} \qquad [7]$$

$nDirs$ is the number of diffusion weighted measurements. $nTerms = (L+1)^2$ is the total number of terms of the SHs through order L, and $nDirs \geq nTerms$ is required to determine $\vec{s}_{lm}$. One way to estimate $\vec{s}_{lm}$ is to minimize the squared fitting error, i.e., $\vec{s}_{lm} = \arg\min(\| \vec{S} - \widetilde{X} \cdot \vec{s}_{lm} \|^2)$. The linear least-squares solution is

$$\vec{s}_{lm} = (\widetilde{X}^T \widetilde{X})^{-1} \widetilde{X}^T \vec{S} \qquad [8]$$

Once the coefficients $\vec{s}_{lm}$ are obtained, the function $\vec{S}$ can be reconstructed from Eq. [6].

Calculation of fiber angular distributions

This section describes how to calculate the fiber angular distribution and perpendicular diffusivity using the FORECAST model. As mentioned above, the diffusion weighted signal measured along direction (θ, φ) can be expressed as a convolution of the fiber angular distribution function $P(\theta', \varphi')$ and the response function from a single ideal fiber:

$$S(tr(\widetilde{b}), \theta, \varphi) = S_0 \int_0^{2\pi} \int_0^{\pi} P(\theta', \varphi') k\left(tr(\widetilde{b}), \overline{\lambda}, \lambda_\perp, \alpha\right) \sin \theta' d\theta' d\varphi' \qquad [9]$$

where $tr(\widetilde{b})$ is the *b value*, S_0 is the un-weighted signal, (θ, φ) are the polar and azimuthal angles of the spherical coordinates. The convolution kernel k depends on the b value, the mean diffusivity $\overline{\lambda}$, the perpendicular diffusivity $\lambda_\perp$ (assuming axially symmetric diffusion tensor) and the angle α between the diffusion gradient direction (θ, φ) and the fiber orientation (θ', φ'):

$$k(tr(\widetilde{b}), \overline{\lambda}, \lambda_\perp, \alpha) = e^{-tr(\widetilde{b})\lambda_\perp} \cdot e^{-3tr(\widetilde{b})(\overline{\lambda} - \lambda_\perp)\cos^2 \alpha} \qquad [10]$$

If the diffusion weighted signal, the fiber angular distribution function and the convolution kernel are all expressed in terms of SHs, then the convolution relationship between the signal S and the FAD P (Eq. [9]) becomes a simple algebraic equation in terms of their SH coefficients $\vec{s}_{lm}$ and $\vec{p}_{lm}$:

$$s_{lm} = S_0 \cdot c_l \cdot p_{lm} \qquad [11]$$

where coefficients c_l are defined as:

$$c_l \equiv \frac{4\pi}{2l+1} e^{-tr(\widetilde{b}) \cdot \lambda_\perp} A_l \qquad [12]$$

The A_l are the lth-order coefficients of the Legendre polynomial expansion of

function $e^{-tr(\tilde{b})\cdot(\lambda_\parallel - \lambda_\perp)x^2}$. The perpendicular diffusivity $\lambda_\perp$ can be estimated from the relation

between the signals, the b value and the presumed mean diffusivity $\bar{\lambda}$:

$$\frac{\bar{S}}{S_0} = \frac{\sqrt{\pi}}{2} \cdot \frac{erf\left(\sqrt{3tr(\tilde{b})\cdot(\bar{\lambda} - \lambda_\perp)}\right)}{\sqrt{3tr(\tilde{b})\cdot(\bar{\lambda} - \lambda_\perp)}} \cdot e^{-tr(\tilde{b})\lambda_\perp} \qquad [13]$$

Once $\lambda_\perp$ and $\vec{c}_l$ are determined from Eq. [13] and [12], respectively, and the SH

expansion coefficients of the diffusion weighted signal $\vec{s}_{lm}$ are obtained through

least-square estimation according to Eq. [8], $\vec{p}_{lm}$ can be determined from Eq. [11], and

the fiber angular distribution function can then be recovered from the SH relationship

according to Eq. [6]. Details of the derivations of $\vec{c}_l$ and $\lambda_\perp$ can be found in (28).

The first step of simulation is to generate the HARD signal. For a voxel

containing a single fiber population along (θ', φ'), the fiber angular distribution $P(\theta, \varphi)$

can be expressed as a symmetric delta function:

$$P(\theta, \varphi) = \frac{1}{2}\left[\delta(\cos\theta - \cos\theta')\cdot\delta(\varphi - \varphi') + \delta(\cos\theta - \cos(\pi - \theta'))\cdot\delta(\varphi - (\pi + \varphi'))\right] \quad [14]$$

Substituting $F(\theta, \varphi) = P(\theta, \varphi)$ in Eq. [4] yields the lth-order FAD coefficients for an

ideal single fiber along (θ', φ') :

$$p_{lm}(\theta', \varphi') = \frac{1}{2}\left[Y_{lm}^*(\theta', \varphi') + Y_{lm}^*((\pi - \theta'), (\pi + \varphi'))\right] \qquad [15]$$

for even l. Since the coefficients $\vec{c}_l$ are determined for given b value, mean diffusivity $\bar{\lambda}$

and perpendicular diffusivity $\lambda_\perp$, the SH coefficients $\vec{s}_{lm}$ can be obtained from relation

[11], and the ideal diffusion weighted signal S can then be reconstructed from the SH

coefficients $\vec{s}_{lm}$ using relation [6].

Even-order-fitting of SH

High order SH approximation is desirable in order to achieve high angular resolution (28) so that fibers with small orientation differences within a voxel can be distinguished. However, the choice of maximum order is limited by the number of the diffusion measurements (note that the number of measurements *nDirs* should be greater than or equal to the number of unknown parameters $(L+1)^2$), which is in turn limited by the total imaging time. Since the signal function, the ideal single fiber response function, and the fiber angular distribution function are all symmetric about the origin, the non-zero odd-order coefficients producing asymmetric components represent the effect of noise. Therefore, we could set all the odd-order SHs coefficients to zero, and solve for only the even-order items. By doing so, the number of coefficients to be determined for an *L* order fit reduces from $(L+1)^2$ to $(L+1)(L+2)/2$. In the remainder of this paper, this method is referred to as even-order-fitting as opposed to the original full-fitting. For a given number of measurements *nDirs*, order *L* denotes the maximum even integer that satisfies the full-fitting condition $nDirs \geq (L+1)^2$. If $nDirs \geq (L+3)(L+4)/2$, we could apply the even-order-fitting at higher order $(L+2)$ for higher angular resolution. If the condition for the higher order $(L+2)$ is not met, using even-order-fitting at order *L* may still improve the noise immunity by reducing the unknown parameters and increasing the degrees of freedom for the least-squares fitting problem. This hypothesis was tested by Monte Carlo simulation.

Tikhonov regularization

One problem of the FORECAST model is that the reconstructed fiber angular distribution may contain negative values in some orientations due to the noise. Because the FAD gives the estimated volume fraction of fibers at each orientation, a negative FAD value is certainly non-physical, and should be minimized. One way to reduce the effect of noise and enhance the solution robustness of the least square problem is to impose additional constraints on the solution. Substituting Eq. [11] into Eq. [6] yields

$$\vec{S} = \tilde{X} \cdot S_0 \cdot \vec{c}_l \cdot \vec{p}_{lm} = \tilde{A} \cdot \vec{p}_{lm} \tag{16}$$

where $\tilde{A} = \tilde{X} \cdot S_0 \cdot \vec{c}_l$. Then the least-square problem becomes

$$\vec{p}_{lm} = \arg\min(\| \vec{S} - \tilde{A} \cdot \vec{p}_{lm} \|^2) \tag{17}$$

To identify the orientations along which the estimated FAD has negative magnitudes, the FAD is estimated in 1002 directions evenly distributed over a sphere (generated by 10th order icosahedral tessellation). Let $\tilde{R}$ be the constraint matrix that maps $\vec{p}_{lm}$ to the amplitude of the FAD (only for those orientations along which the estimated FAD has negative values) so that $\tilde{R} \cdot \vec{p}_{lm}$ is the sum of the negative FAD values. The regularized $\vec{p}_{lm}$ should minimize not only the estimation errors, but also the negative FAD values, satisfying

$$\vec{p}_{lm} = \arg\min(\| \vec{S} - \tilde{A} \cdot \vec{p}_{lm} \|^2 + \omega^2 \| \tilde{R} \cdot \vec{p}_{lm} \|^2) \tag{18}$$

where ω is a weighting factor for balancing the two terms. The least-squares solution of Eq. [18] is

$$\vec{p}_{lm} = (\widetilde{A}^T \widetilde{A} + \omega^2 \widetilde{R}^T \widetilde{R})^{-1} \widetilde{A}^T \vec{S} \qquad\qquad [19]$$

Regularization effects depend on the choice of the weighting factor ω. One way to determine the optimal ω is the L-curve method (51). In this study, various values of ω were tested on the data simulated using different imaging and analysis parameters, and the optimal ω for each condition was determined based on the several figures of merit.

FADs estimated at different maximum orders may show different negative magnitudes along different orientations, leading to different constraint matrices $\widetilde{R}$ and different regularization results. Theoretically speaking, the higher the SH order is, the higher the angular frequency components it represents and the more sensitive to noise the fitting is. In this study, we tested the regularization algorithm in two different configurations. In the first configuration, referred to same-order regularization, the regularization term is based on the FAD estimated to the same order as the fitting error term, i.e., the highest order L of the SHs in the matrix $\widetilde{A}$ is same as that in matrix $\widetilde{R}$. In the second configuration, termed lower-order regularization, the maximum order of the SHs in matrix R is *(L-2)* instead of L. Lower-order regularization has been proposed by Tourier et al. (52).

Simulation procedure

Two groups of intravoxel structures were simulated, a single fiber and two crossing fibers. For the single fiber case, three fibers orientated along x, y, and z axes, respectively, were

simulated. For the crossing fibers case, two fibers with the same volume fraction both lie in the x-y plane, with the crossing angle ranging from 60º to 90º. For fiber #1, $(\theta_1, \varphi_1) = (90°, 30°)$. Fiber #2 has the same θ, with φ depending on the crossing angle (see figure 2). For each structure, different values of the three imaging parameters were tested ($tr(\widetilde{b})$=1000, 2100, and 3250s/mm^2, number of diffusion gradient directions *nDirs*=32 or 92, and SNR varied from 10 to 100). For each combination of the given structure and imaging parameters, 500 Monte Carlo simulations were performed, for each resulting dataset, FORECAST analysis using various parameters were applied, including the fitting order (4th order, or 6th order), the fitting method (full-fitting or even-order-fitting), the regularization order (same-order or lower-order), and the regularization weighting factor (ω ranging from 0.0001 to 1). The mean, standard deviation and other statistics of the figures of merit (discussed later) for each configuration were compared.
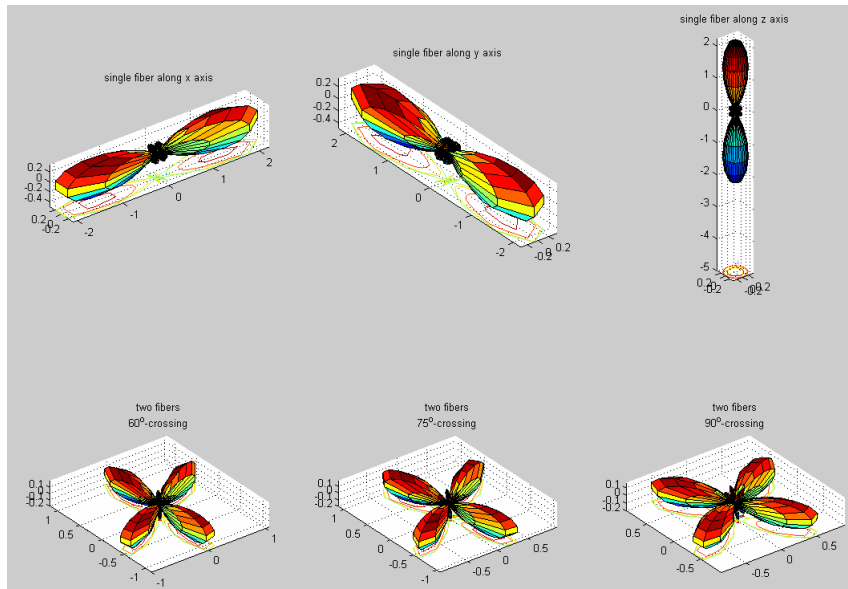
Figure 2. Examples of FADs showing the simulated intravoxel fiber structures

22

The simulation procedure is summarized as the following steps:

1. Set mean diffusivity and perpendicular diffusivity. In this study, they were chosen as $\bar{\lambda} = 0.9 \times 10^{-3} mm^2 / s$, and $\lambda_{\perp} = 0.6 \times \bar{\lambda}$, respectively, which are typical values for human brain white matter.

2. Set b value (choosing from 1000, 2100, and 3250s/mm^2).

3. Set fitting order (4th order or 6th order).

4. Set number of diffusion gradients, and generate this number of gradients vectors uniformly distributed over a unit sphere. In this study 92 gradient directions given by 3rd order icosahedral tessellation of the unit sphere, and 32 directions used by the Philips scanner system (see Appendix A) were tested.

5. Set fitting method (full-fitting or even-order-fitting), then construct corresponding SHs design matrix.

6. Set the intravoxel architecture, determine the ideal fiber(s)' orientations.

7. Calculate the ideal FAD coefficients $\vec{p}_{lm}$ from Eq. [15], then reconstruct the ideal diffusion signals and derive parameters of the ideal structure for later comparison. Normalize the ideal signals so that the un-weighted signal, S_0, has value 1.

8. Set SNR level (ranging from 10 to 100), add random noise with zero mean and standard deviation of 1/SNR to the ideal signals.

9. Perform FORECAST analysis on the noisy signal to estimate the FAD, $\lambda_{\perp}$ and other parameters of interest.

10. Set regularization method (same-order or lower-order) and the weighting factor ω (0.0001 to 1), perform regularization, and then recalculate the figures of merit based on the regularized $\vec{p}_{lm}$.

11. Using the same parameter settings, repeat steps 8 to 10 for a total of 500 trials.

12. Calculate the mean, standard deviation or other statistics of the measures for each un-regularized and regularized configuration.

13. Change one of the parameters (fiber, acquisition, or analysis) and repeat steps 2 to 12, until try out all the options have been run.

14. Compare the results between the ideal data, un-regularized data and regularized data.

Figures of merit for performance evaluation

When evaluating an estimated FAD, the following aspects are considered: the number of detected fiber bundles, the angular error in estimated fiber bundle orientation, the overall shape of the FAD, and the volume fraction of each fiber bundle. In this part, several figures of merit used for the performance evaluation are introduced.

The angular deviation of the FAD peaks from the true fiber orientations

The mean and the standard deviation of this value over all the trials indicate the angular accuracy and precision of the FORECAST model. Once the SH coefficients of the FAD

were obtained, FAD could be estimated along a grid of 12800 orientations defined by 80 different θ angles ranging from 0º to 90º, and 160 different φ angles ranging from 0º to 360º. The distinct peaks of the FAD could be located among these sampled points. In the single fiber case, if the estimated FAD contained more than one peak, the peak with the largest amplitude was considered to be the estimated fiber orientation. In the two-fiber cases where the estimated FAD may have one or multiple peaks, in order to calculate the deviation from the set of ideal orientations, it needed to be determined which of the estimated fiber(s) corresponded to each of the ideal fibers. This was done by enumerating all the possible correspondences, then for each case calculating the sum of the angle difference for each corresponding orientation. The correspondence with the smallest total angular difference was then chosen. The angular deviation for each fiber was summed for comparison.

The Angular Correlation Coefficient (ACC) between the estimated FAD and the ideal FAD

The ACC is a natural similarity measure concerning both the shape and orientation between two spherical functions, ranging from -1 (perfect negative correlation) to 1 (exactly identical). According to our preliminary studies, an ACC value of at least 0.8 is desirable for estimation of the FAD. Due to the linear relationship between a spherical function and its SH coefficients, the ACC between two FADs can be calculated from the correlation coefficient between the two SH coefficient vectors. The mean and standard

deviation of the ACC over the 500 trials were compared for each configuration.

The probability of correctly estimating the number of fiber bundles

This figure of merit checks if the estimated FAD indicates any false fiber bundles. If the estimated FAD contained more than one peaks, and the magnitude of a certain peak was too small relative to the largest one within the same voxel, this peak was considered false, produced by either imaging noise or truncation artifact from the SH fitting. Those false peaks were ignored. The magnitude ratio threshold was set to 1/5 to best catch the false peaks based on our preliminary results. For each configuration, the chance of resolving the true number of fiber bundles (the fraction of 500 trials) was recorded and compared.

Another aspect of this figure of merit is the ability to resolve multiple fibers within a voxel. The important question is how small the crossing angle between the orientations of two fibers can be in order for them to be resolved by the FORECAST model. The answer depends on the fitting order and the SNR of the data. Without the effects of noise, the higher the fitting order, the higher the angular resolution. Simulation results (see figure 3) show that in the noise-free situation, the minimum crossing angle that the FORECAST model is able to resolve is about 55º using 4th order fitting and 40º using 6th order fitting. In this study, focus was put on comparing the abilities of revolving 60º crossing fibers under various configurations. Though analysis on structures of other crossing angles was also performed, the results are not shown or discussed in this report.
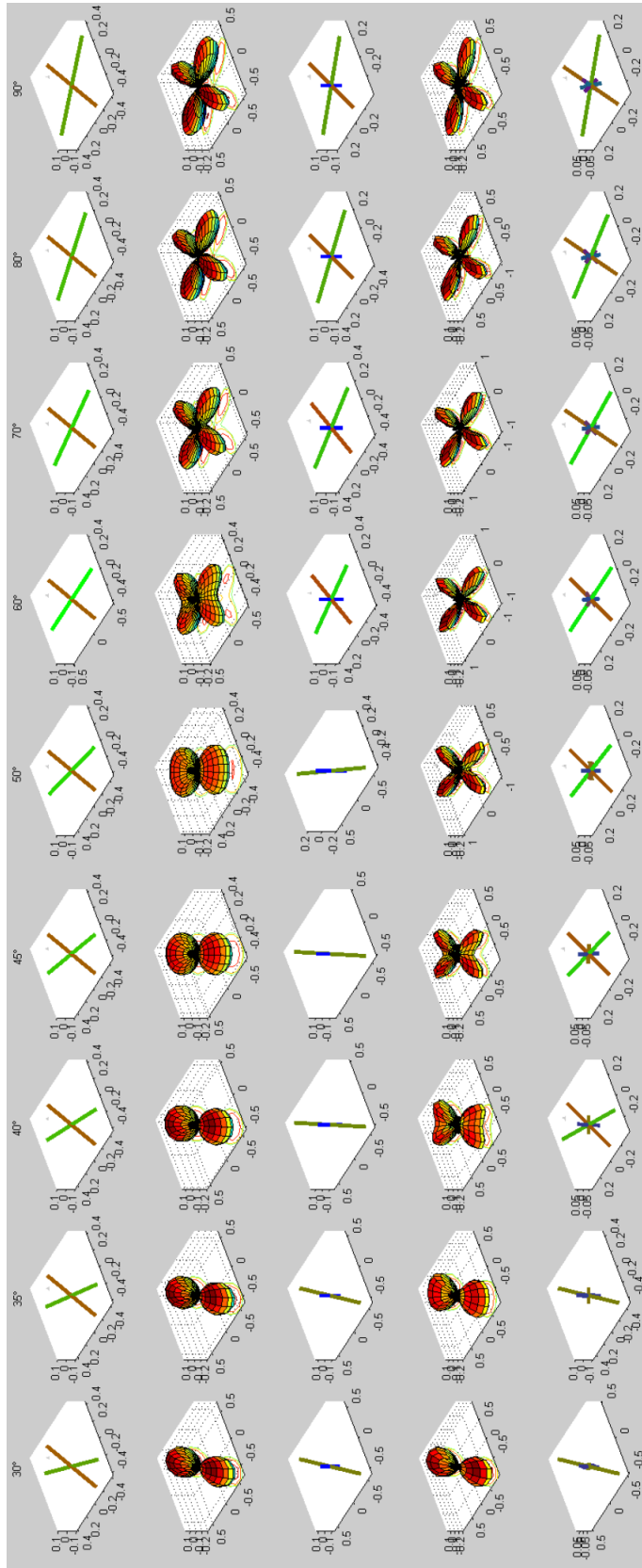
Figure 3. The ability of the FORECAST model to resolve two crossing fibers under noise-free situations. The top row shows the stick model of the fiber orientations, which is color-encoded (red, green, blue indicates x, y, z directions, respectively). Both fibers lie in the x-y plane. Fiber #1 (the brown one) is orientated 30° from the x-axis, and the orientation of fiber #2 (the green one) varies as the crossing angle increasing from 30° to 90° (each column from left to right). The next two rows show the FADs reconstructed from the 4th order and the corresponding stick models indicating the FAD peak. The bottom two rows are results from the 6th order reconstruction.

The Volume fraction for fiber #1 in the two-fiber cases where more than one FAD peaks were found

Since the volume fraction for each ideal fiber was set to be same, comparing one of them should be sufficient. The mean of the volume fractions for fiber #1 over 500 trials was compared for each two-fiber configuration.

Note that the figure of merit of the number of fiber bundles should be considered along with the volume fraction and the angular deviation for the two-fiber structure. Since the image noise and truncation artifact may result in false fibers with magnitude larger than the threshold, a correct estimate of the number of fibers does not necessarily mean a good estimate without a close volume fraction and small angular error.

Human data acquisition and analysis

In addition to the numerical simulation, we also validated the techniques using *in vivo* human data. HARD data from a normal control was acquired on a Philips 3T scanner with informed consent. The dataset contains $96 \times 96 \times 55$ isotropic voxels at the spatial resolution of 2.5 mm. Diffusion weighting ($tr(\widetilde{b})$=1000s/mm^2) was applied along 92 directions given by the 3rd order icosahedral tessellation (total scan time of 17 minutes).

FORECAST analysis was performed using mean diffusivity $\bar{\lambda} = 0.9 \times 10^{-3} mm^2 / s$ for the whole dataset and perpendicular diffusivity $\lambda_\perp$ optimized for each voxel. Tikhonov regularization using the optimal parameters determined by simulation results (shown in the next chapter) was applied. In addition to the

regularization, another de-noising technique, the anisotropic smoothing developed by Ding et al. (53), was tested. By adjusting the smoothing kernel according to the structural homogeneity along each measurement direction, this technique is able to smooth within fiber bundles while preventing boundary blurring between different bundles (53). In order to evaluate the effect of the regularization and the smoothing algorithm, FADs estimated with regularization and without regularization, before smoothing and after smoothing were compared.

CHAPTER III

RESULTS

Results of both the numerical simulation and *in vivo* human data are presented below.

Results of simulations

Figures 4, 5, and 6 show the effects of the analysis parameters on performance in single

and two-fiber structures. Figures 7 and 8 show the effects of the imaging parameters on

performance. Each figure of merit is shown in one subplot.

Effect of the fitting method

It is obvious in all the subplots of figures 4 and 5 that 4th order full-fitting (green lines)

and the corresponding 4th order even-order-fitting (blue lines) overlap for most of the ω

values. The same pattern is observed in each dataset acquired with 92 diffusion directions,

no matter what *b* value and regularization method was applied (results not shown). These

results indicate that with 92 measurements, the performance difference between 4th order

full-fitting and 4th order even-order-fitting is negligible. However, these two fitting

methods give different results in 32-direction measurements, as seen in figure 6.

Comparing the results without regularization, or with same-order regularization, the 4th order even-order-fitting gives lower angular deviation and higher ACC value than the 4th order full-fitting. Therefore, the effect of the fitting method interacts with both the number of diffusion encoding directions and the regularization methods.

Figures 4, 5, and 6 also demonstrate that compared with 4th order fitting, the 6th order even-order-fit gives worse ACC performance (lower mean and higher standard deviation), together with higher minimum angular deviation (i.e., the minimum as a function of the regularization parameter ω) in both single fiber and two-fiber structures. Note that the 6th order fitting provides more accurate estimates of the number of fibers and fiber volume in the multi-fiber case.

Effect of regularization

As illustrated in figures 4 and 5, with the proper choice of the regularization order and the weighting factor ω, regularization is able to improve FORECAST performance in terms of a lower angular deviation, higher ACC value and more accurate estimate of the number of fibers. In general, the higher the *b* value, and/or the higher the SNR, the smaller the ω needed. For example, data generated using 92 measurements at b=1000s/mm², SNR=40, and analyzed using 4th order fitting, lower-order regularization with ω=0.01 is nearly optimal.

For the single fiber data (shown in figure 4), lower-order regularization always

outperforms the same-order regularization compared at matching imaging configurations, though the difference is much smaller for the 4th order fitting than the 6th order fitting. Also, the difference becomes smaller as the SNR increases (comparison of different SNR data not shown). Similar results are observed for the two-fiber structure analyzed using 6th order fitting. For 4th order fitting (shown in figure 5), however, in terms of volume fraction and number of detected fibers, the two regularization methods make no obvious difference with ω less than 0.01. As ω increases, the lower-order regularization yields larger error on volume fraction and the estimated number of fibers compared to same-order regularization. The lower mean ACC and larger ACC standard deviation also indicate that the solution is over-regularized with high ω.

The optimal analysis parameters are summarized in table 1.

Table 1. Optimal analysis parameters: fitting order, regularization method (S: same-order regularization, L: lower-order regularization, and the regularization weighting factor ω).

Measurement number	b value (s/mm^2)	SNR					
		10	20	30	40	50	60
92	1000	4, S, 0.11	4, L, 0.03	4, L, 0.03	4, L, 0.01 or 6, L, 0.03		
	2100	4, S, 0.11	4, S, 0.05	4, S, 0.03	4, L, 0.03 or 6, L, 0.03		
	3250	4, S, 0.03	4, S, 0.03	4, S, 0.03	4, L, 0.01 or 6, L, 0.03		
32	1000	4, S, 0.09	4, S, 0.03	4, S, 0.03	4, L, 0.01		
	2100	4, S, 0.07	4, S, 0.05	4, S, 0.03			
	3250	4, S, 0.01	4, S, 0.03	4, S, 0.03			
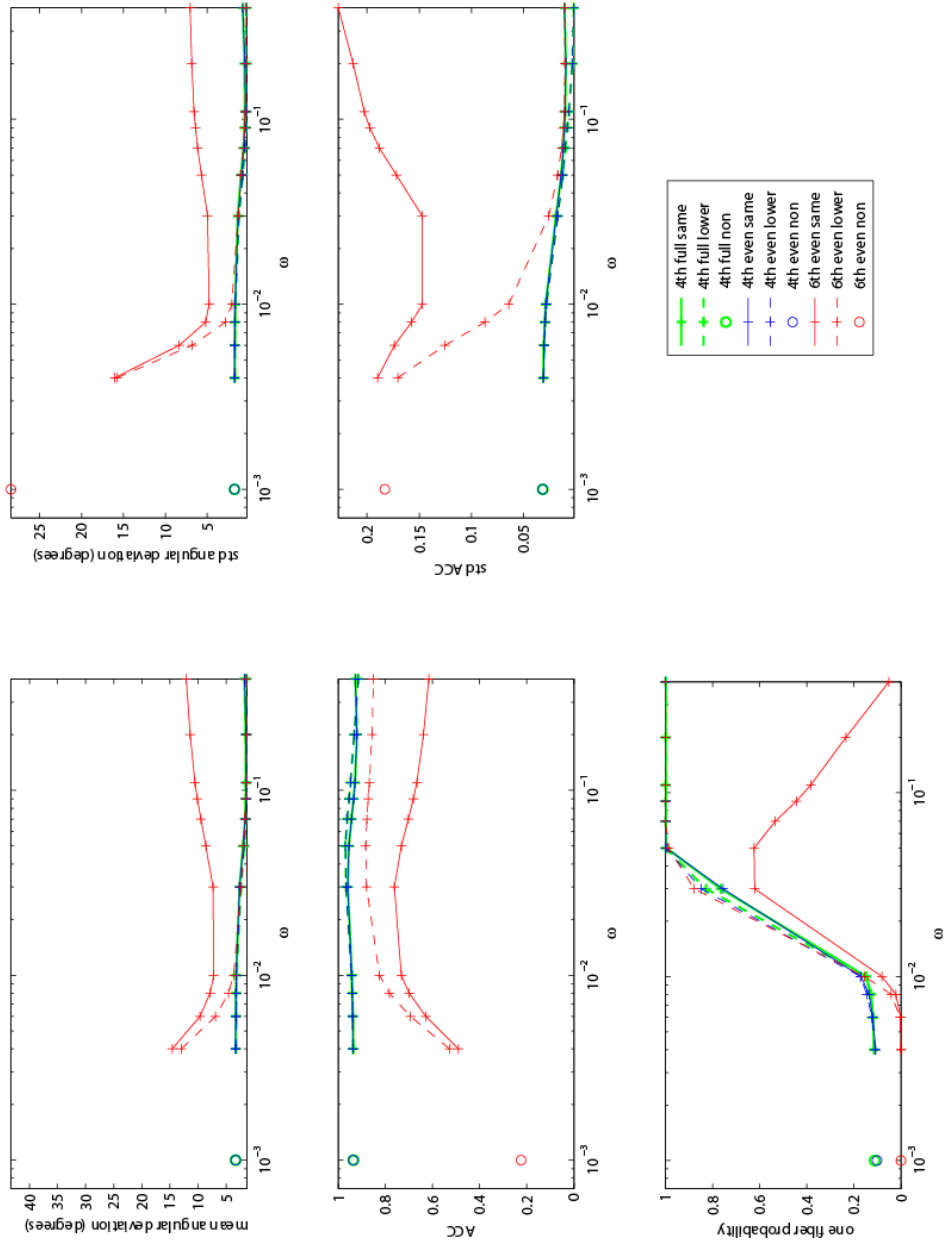
Figure 4. Performance dependence on analysis parameters for a single fiber oriented along (90°, 0°), data acquired using 92 diffusion directions at b=1000s/mm^2 and SNR=40. Each subplot shows one evaluation figure of merit $vs.$ ω for various fitting methods and regularization schemes. In each subplot, green, blue, and red denotes 4th order full-fitting, 4th order even-order-fitting, and 6th order even-fitting, respectively. Solid lines denote same-order regularization, dashed lines denote lower-order regularization, and circles denote results from non-regularized data.

34
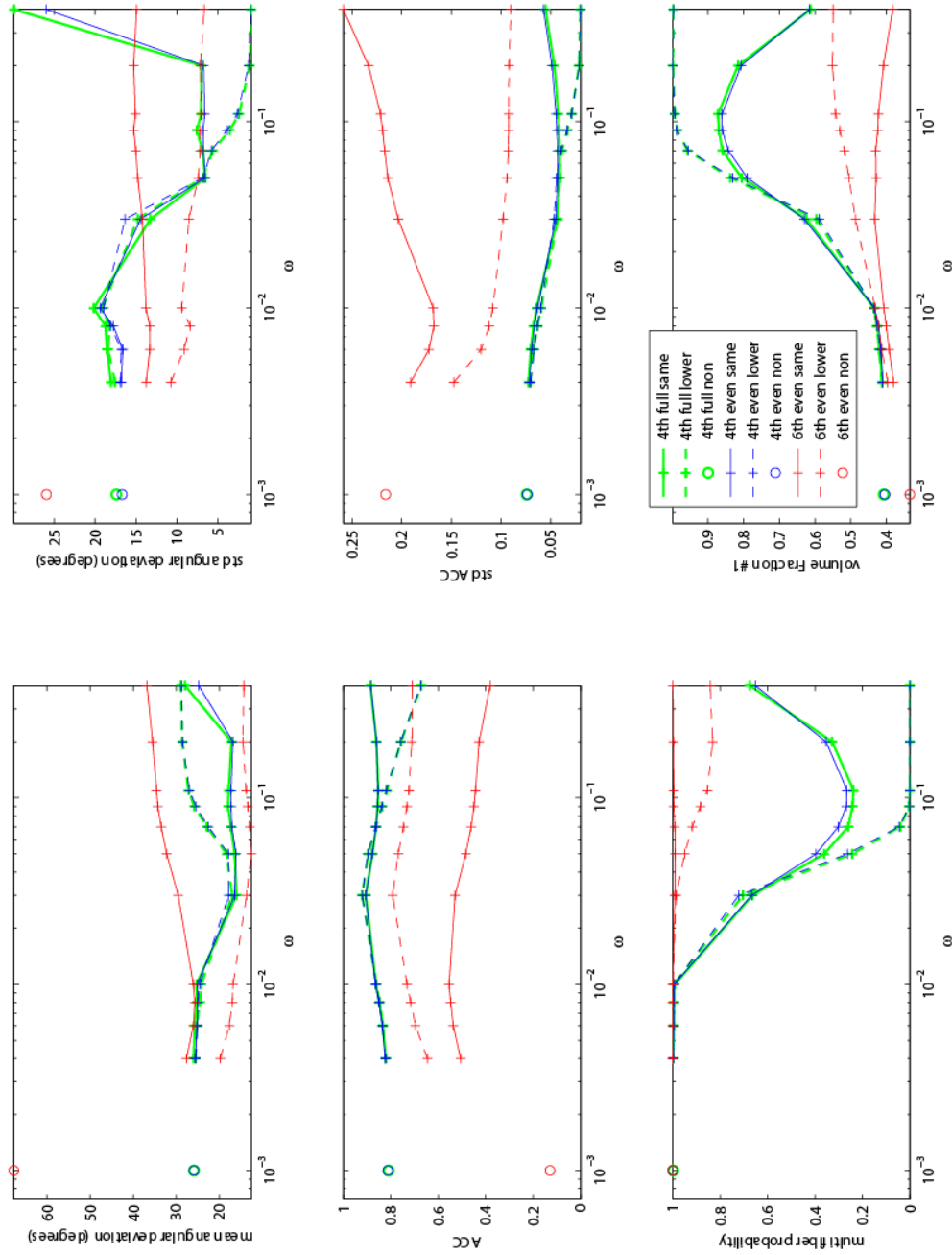
Figure 5. Performance dependence on analysis parameters for two fibers crossing at 60°, data acquired using 92 diffusion directions at b=1000s/mm^2 and SNR=40. Each subplot shows one evaluation figure of merit *vs.* ω for various fitting and regularization schemes. In each subplot, green, blue, and red denotes 4th order full-fitting, 4th order even-order-fitting, and 6th order even-fitting, respectively. Solid lines denote same-order regularization, dashed lines denote lower-order regularization, and circles denote results from non-regularized data.

35
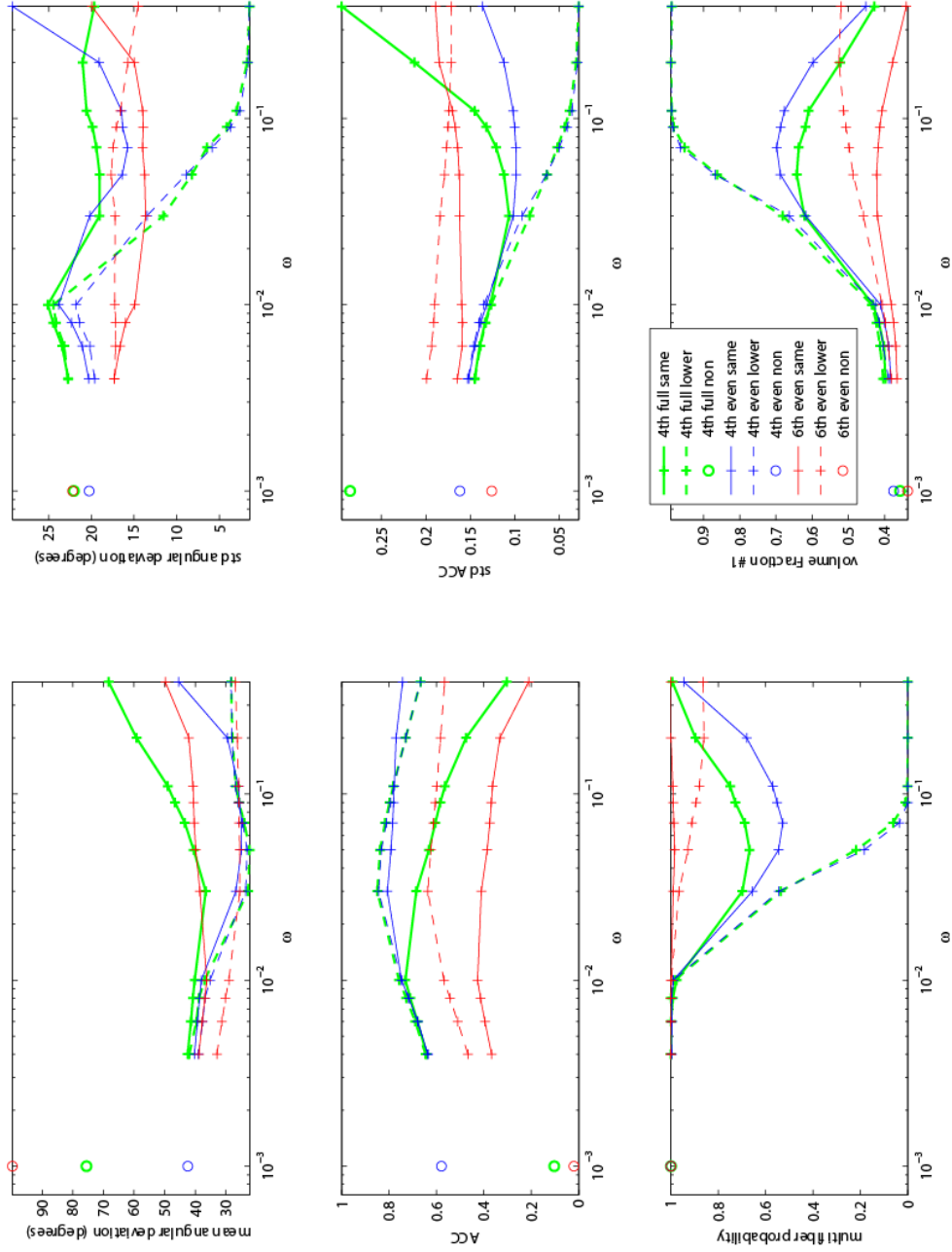
Figure 6. Performance dependence on analysis parameters for two fibers crossing at 60°, data acquired using 32 diffusion directions at b=1000s/mm^2 and SNR=40. Each subplot shows one evaluation figure of merit vs. ω for various fitting and regularization schemes. In each subplot, green, blue, and red denotes 4th order full-fitting, 4th order even-order-fitting, and 6th order even-fitting, respectively. Solid lines denote same-order regularization, dashed lines denote lower-order regularization, and circles denote results from non-regularized data.

36

Effect of the number of diffusion directions

By comparing the solid lines (denoting the 92-direction measurement) to the same-color dashed lines (denoting the 32-direction measurement) in each subplot of figure 7 (single-fiber structure) and figure 8 (two-fiber structure), it is obvious that the 92-direction measurement almost always yields better results than the 32-direction measurement, in terms of the lower angular deviation, higher ACC and more accurate estimate of the number of fibers.

Effect of the b value

As seen in Figures 7 and 8, when analyzed at 4th order, data generated using $b = 2100s/mm^2$ outperforms data generated using lower (1000s/mm^2) or higher (3250s/mm^2) b values, in terms of the lower angular deviation, higher ACC and more accurate estimate of the number of fibers.

Effect of SNR

As shown in figures 7 and 8, the higher the SNR, the lower the angular deviation, the higher the ACC and the higher the detection rate of multiple fibers.
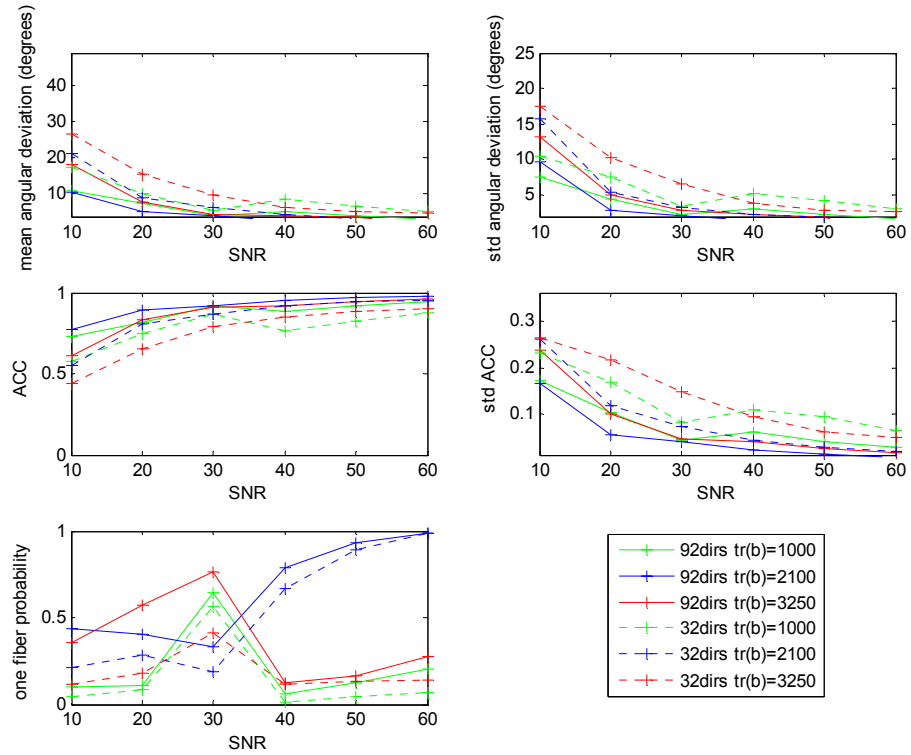
Figure 7. Performance dependence on imaging parameters for a single fiber oriented along (90º, 0º). Each subplot shows one figure of merit vs. SNR at various measurement numbers and *b* values. In each subplot, solid lines denote 92-direction, dashed lines 32-direction measurements. Green, blue, and red denote *b* values of 1000, 2100 and 3250s/mm^2, respectively. All the data were processed using the optimal fitting method and regularization method chosen for each configuration (Table 1).
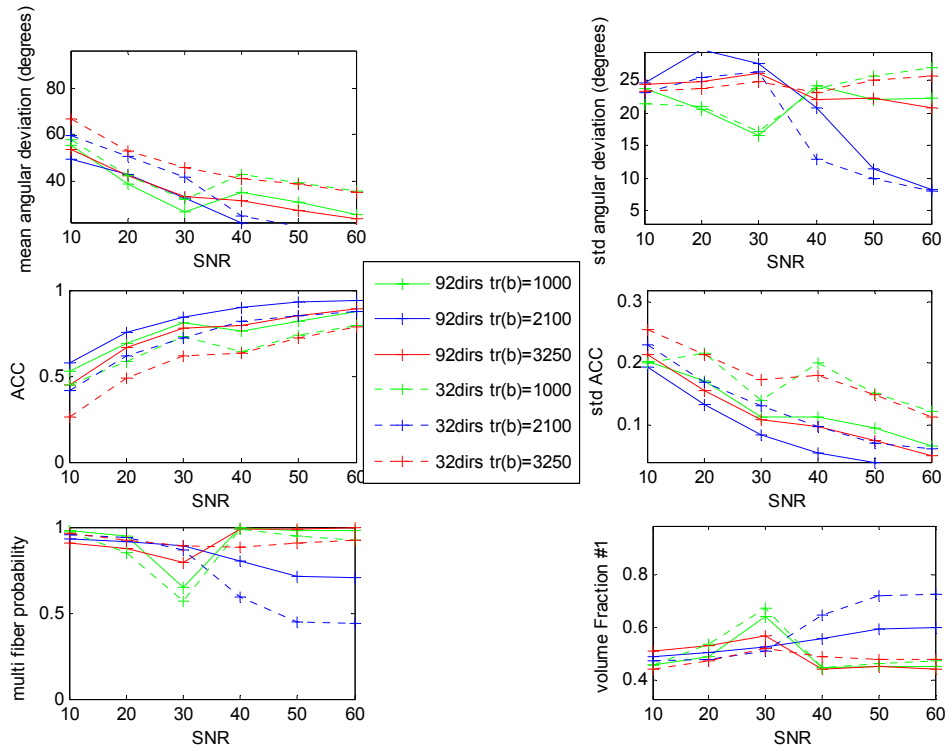
Figure 8. Performance dependence on imaging parameters for two fibers crossing at 60º. Each subplot shows one figure of merit vs. SNR at various measurement numbers and *b* values. In each subplot, solid lines denote 92-direction and dashed lines 32-direction measurements. Green, blue, and red denote *b* values of 1000, 2100 and 3250s/mm^2, respectively. All the data were processed using the optimal fitting method and regularization method chosen for each configuration (Table 1).

Results of the human data

FORECAST analysis was performed on the *in vivo* dataset acquired. SNR was estimated to be about 40 based on the Residual Sum of Squares (RSS). According to the simulation results, the optimal analysis parameters were chosen as follows: 6th order even-order-fitting and lower-order regularization with $\omega = 0.03$. A Region Of Interest (ROI) with voxels containing no fibers, a single-fiber, and multiple fibers was chosen. As shown in the top of the figure 9, the ROI includes part of the ventricle (*vtc*) demonstrating isotropic diffusion, several fiber bundles demonstrating single-fiber anisotropic diffusion, and regions demonstrating complex diffusion where two or more fiber bundles cross. These fiber bundles include the corpus callosum (*cc*) which mainly goes in the left-right direction, the cingulum bundle (*cg*), the superior fronto-occipital fasciculus (*sfo*), the anterior thalamic radiation (*atr*) and the superior longitudinal fasciculus (*slf*) which go in the anterior-posterior direction, the corticopontine tract (*cpt*) and the corticospinal tract (*cst*) which go in the inferior-superior direction. The estimated FADs (figures 9 and 11) and the corresponding stick models indicating the FAD peaks (figures 10 and 12) are shown to demonstrate the effects of regularization and anisotropic smoothing.

By comparing the FADs estimated with and without regularization, figure 9 shows clearly that regularization enhances the FORECAST model's robustness to noise, making the results more reliable. Before regularization, the spiky FADs make it hard to

distinguish the fiber bundles. After regularization, the effect of noise is significantly reduced, and the orientation of each of the major fiber tracts in the ROI is revealed. For example, before regularization, the FADs of the *sfo* tract show some peaks oriented in the left-right direction (see the green ellipses in figures 9 and 10), though there is no fiber nearby going in that direction, based on the known anatomy. To the right (left in the image) of the tract is the ventricle without fibers and to the left (right in the image) is the inferior-superior oriented *cpt/cst* tracts (see the purple ellipses in figures 9 and 10). Therefore, these small FAD peaks may stem from noise. After regularization, these false distributions are minimized, though not completely removed due to truncation artifact. Another example of the ability of regularization to minimize false peaks is shown in the middle of the *cc* tract (see the red ellipses in figures 9 and 10).
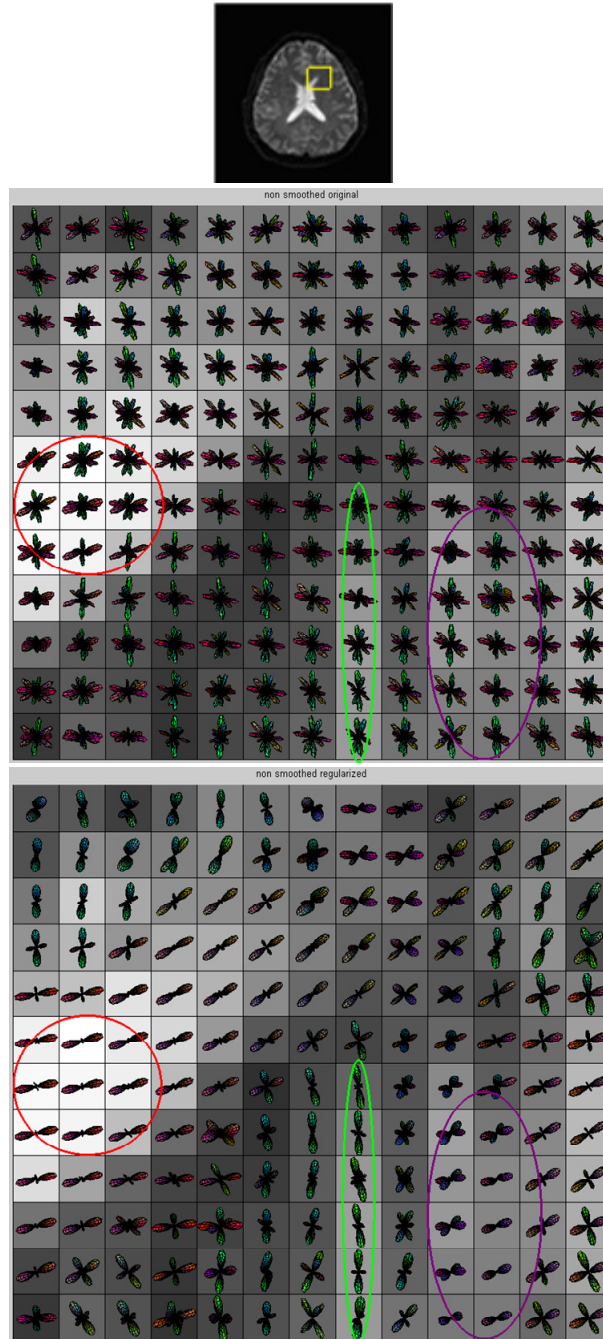
Figure 9. FADs etimated using the FORECAST analysis of an *in vivo* dataset, showing the effect of regularization. Top: The Region Of Interest (ROI) defined as the yellow box on an axial slice of the non-diffusion-weighted image. Middle: FAD surfaces on top of the FA map estimated by the FORECAST model with 6th order even-order-fitting, without anisotropic smoothing or regularization. Bottom: FADs on top of the FA map in the same ROI, estimated after lower-order regularization (ω=0.03). FADs are color-encoded (red: left-right; green: anterior-posterior; blue: inferior-superior). The FA map is gray-scaled. The red, green, and purple ellipses show the *cc*, *sfo*, and *cpt/cst* tracts, respectively.
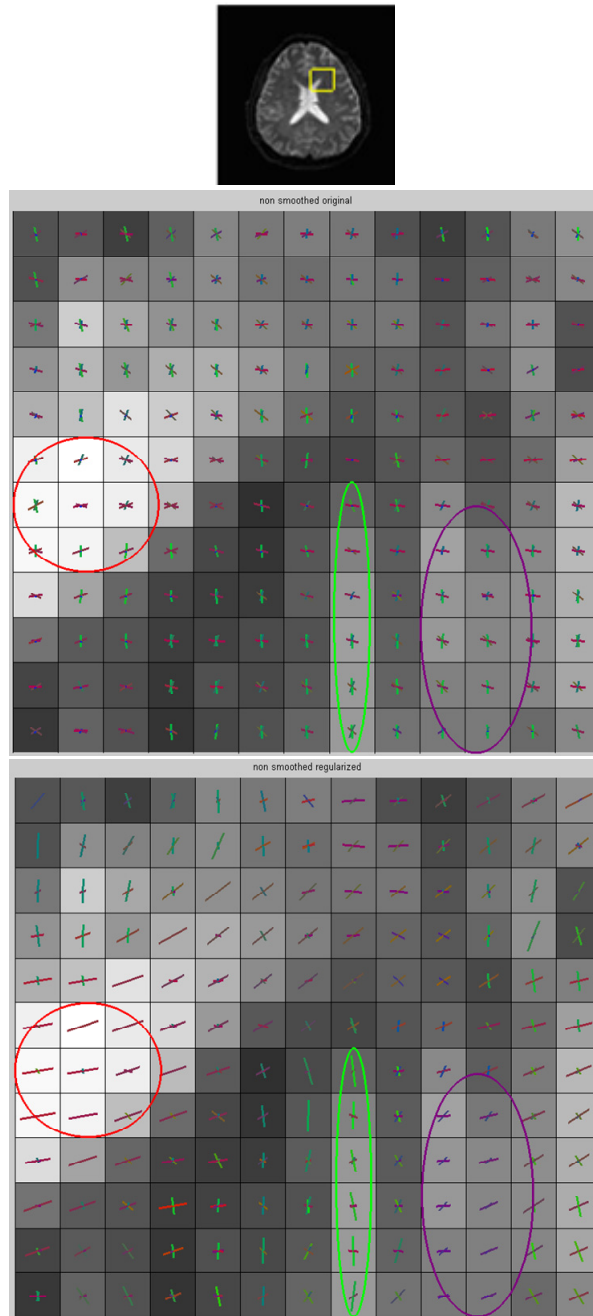
Figure 10. Stick model of the FAD peaks corresponding to the results shown in figure 9. Top: ROI defined as the yellow box on an axial slice of the non-diffusion-weighted image, same as that in figure 9. Middle: stick models on top of the FA map, estimated by FORECAST with 6th order even-order-fitting, without anisotropic smoothing or regularization. Bottom: stick model on top of the FA map in the same ROI, estimated after lower-order regularization (ω=0.03). Orientations of the sticks are color-encoded (red: left-right; green: anterior-posterior; blue: inferior-superior), the lengths of the sticks are proportional to the volume fraction of the estimated fibers. The FA map is gray-scaled. The red, green, and purple ellipses show the *cc*, *sfo*, and *cpt/cst* tracts, respectively.

Figures 11 and 12 illustrate the effect of anisotropic smoothing. Taking the example of the *sfo* tract (see the green ellipses in figures 11 and 12), it is obvious that after smoothing, the principal orientation of each voxel along the tract becomes slightly more coherent than before smoothing.
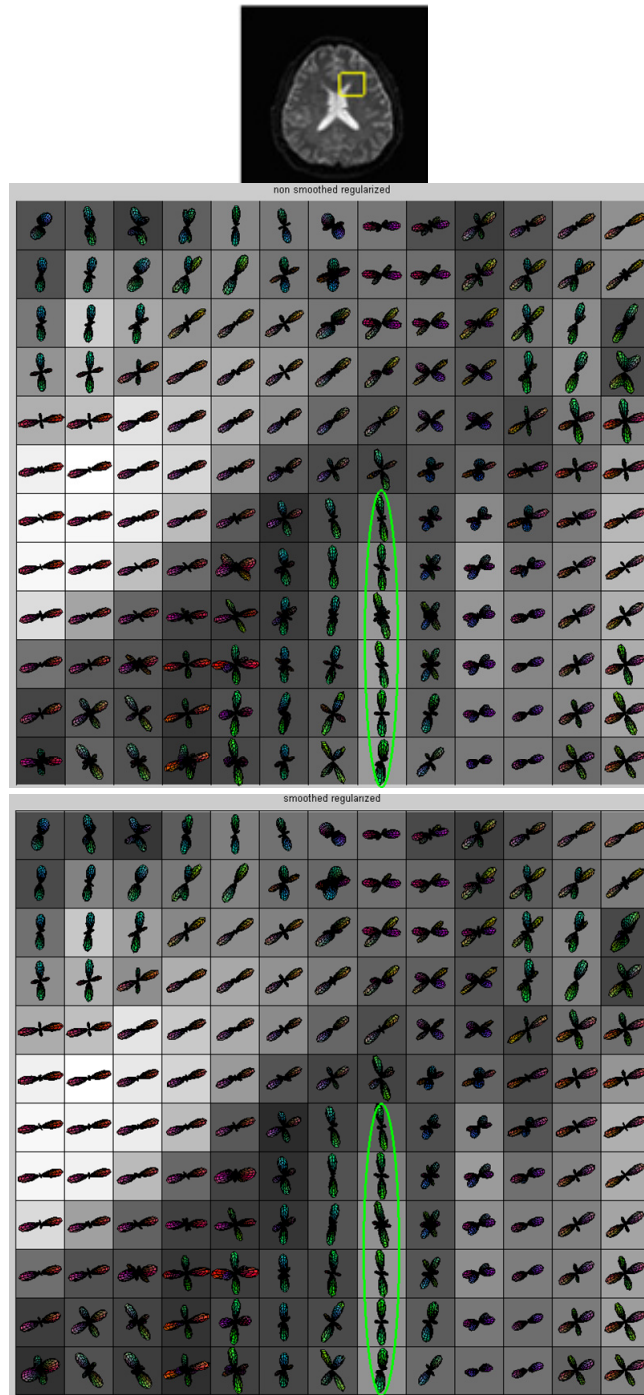
Figure 11. FADs etimated using the FORECAST analysis of the *in vivo* dataset, showing the effect of anisotropic smoothing. Top: ROI defined as the yellow box on an axial slice of the non-diffusion-weighted image, same as that in figure 9. Middle and bottom: FAD surfaces on top of the FA maps, estimated before and after anisotropic smoothing, respectively. They are both analyzed with 6th order even-order-fitting, and lower-order regularization with $\omega=0.03$. FADs are color-encoded (red: left-right; green: anterior-posterior; blue: inferior-superior). The FA map is gray-scaled. The green ellipse shows the *sfo* tract.
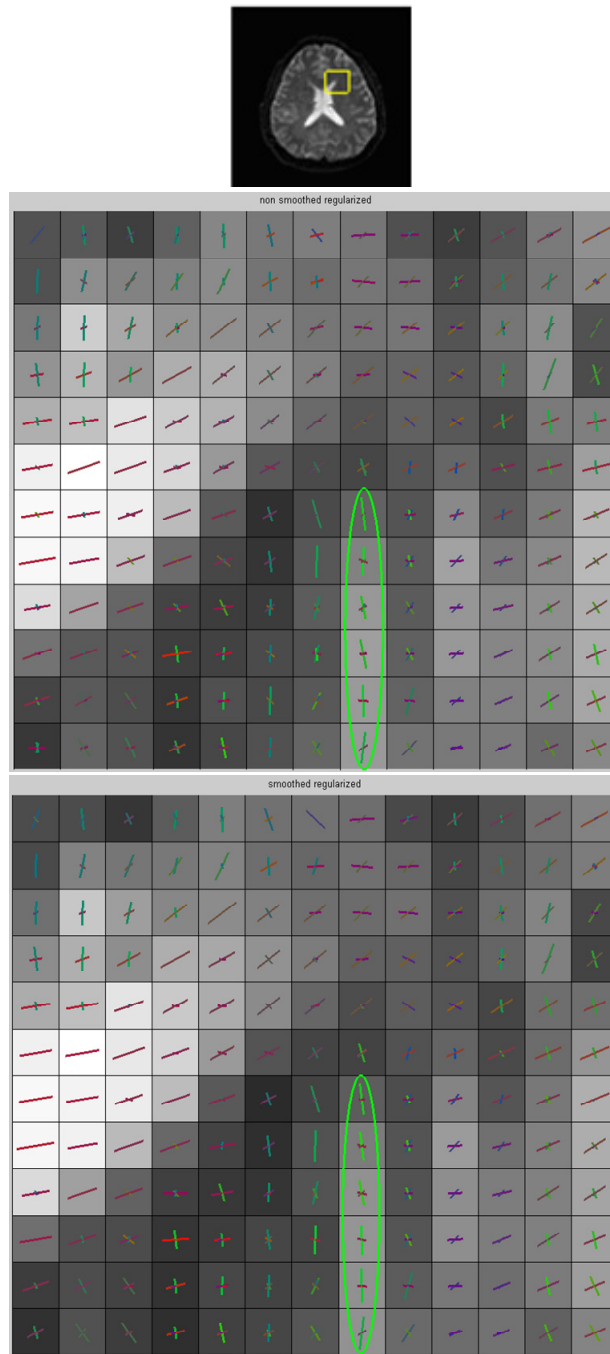
Figure 12. Stick model of the FAD peaks corresponding to the results shown in figure 11. Top: ROI defined as the yellow box on top of an axial slice of the non-diffusion-weighted image, same as that in figure 9. Middle and bottom: the stick model on top of the FA maps, estimated before and after anisotropic smoothing, respectively. They are both analyzed with 6th order even-order-fitting, and lower-order regularization with ω=0.03. Orientations of the sticks are color-encoded (red: left-right; green: anterior-posterior; blue: inferior-superior), the lengths of the sticks are proportional to the volume fraction of the estimated fibers. The FA map is gray-scaled. The green ellipse shows the *sfo* tract.

The results after regularization and smoothing also demonstrate that in regions where fiber bundles with different orientations cross, the FORECAST model is able to distinguish the fiber components (shown in figure 13). For example, in the voxels containing both *cc* fibers and *cg* fibers, the estimated FADs show clearly two peaks oriented in the left-right and anterior-posterior directions, respectively, indicating the orientation of the two fiber bundles (see the blue rectangle in figure 13). In the area where the *cc*, *cpt/cst*, and *atr* tracts meet, the FADs exhibit three distinct peaks each giving the principal orientation of these tracts (see the orange rectangle in figure 13).
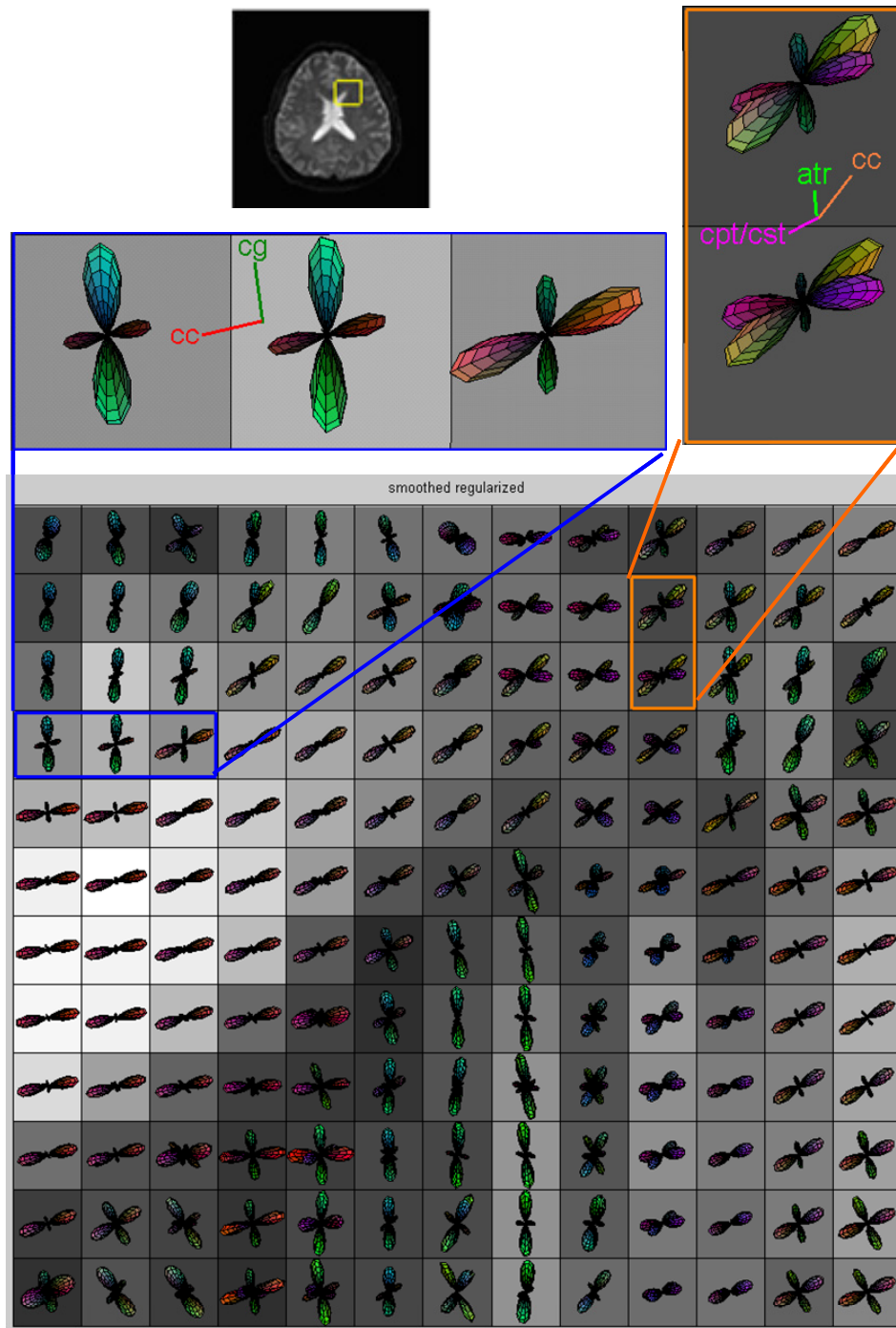
Figure 13. FADs etimated using the FORECAST analysis of the *in vivo* dataset, showing multiple-fiber crossing. Top left: ROI defined as the yellow box on an axial slice of the non-diffusion-weighted image, same as that in figure 9. Bottom: FAD surfaces on top of the FA maps. The magnified blue and orange rectangle demonstrates the two-way and three-way fiber crossing, respectively. Data were analyzed with anisotropic smoothing, 6th order even-order-fitting and lower-order regularization with ω=0.03. FADs are color-encoded (red: left-right; green: anterior-posterior; blue: inferior-superior). The FA map is gray-scaled.

CHAPTER IV

DISCUSSION

Discussion on the results

The simulation results indicate that the 4th order FORECAST analysis is able to provide

reliable estimates of fiber orientation, at least for no more than two fibers in a voxel, and

in the b value and SNR ranges tested. In theory, high order SHs contain high spatial

frequency components of the approximated functions. Therefore, the higher the fitting

order, the narrower the angular point spread function, and the higher the angular

resolution. On the other hand, the HARD measurement is sensitive to noise. The higher

order the fitting, the more sensitive will be the results to high frequency noise. The

simulation results demonstrate that at the low b value of 1000s/mm^2, 6th order fitting

produces higher angular deviation and lower ACC than 4th order fitting without

regularization, though the differences become smaller as b value and SNR increase. The

higher fitting order does not bring the expected benefits of higher angular accuracy

probably because of its higher sensitivity to noise. To overcome the effect of noise and

achieve satisfactory results with the 6th order fitting, higher b value and/or higher SNR is

required. With data acquired at low b value and low SNR, one way to improve the

estimation is Tikhonov regularization. The simulation results demonstrate that

regularization is able to lower the angular error and increase the ACC (this effect is prominent at low b value and low SNR). For example, for the 60º-crossing-fiber structure acquired using 92 diffusion directions, b=1000s/mm^2 and SNR=40, 6th order fitting with proper regularization is able to reach an angular error of 14º compared to 26º by the 4th order fitting without regularization and 25º with proper regularization (as shown in figure 5).

As mentioned in the METHODS section, even-order-fitting is expected to be more accurate because it reduces the number of parameters needed to solve in the over-determined fitting problem. However, the simulation results demonstrate that with 92 diffusion measurements the 4th order full-fitting gives roughly the same results as the 4th order even-order-fitting. One possible reason is that the degrees of freedom for full-fitting (92-25=67) are large enough to overcome the benefit from the relatively small increase of the degrees of freedom (25-15=10) from the even-order-fitting. In the 32-measurement case, however, the benefit of the even-order-fitting is significant since the increase of the degrees of freedom is large (from 7 to 17) relative to the small number of measurements.

The key problem associated with regularization is the choice of the weighting factor ω. The optimal value of ω depends not only on the regularization method, but also on the imaging parameters such as the b value, number of diffusion measurements and SNR, and on the fitting method, as well. Also, choosing the optimal ω is a trade off between all the figures of merit. For example, for two fibers crossing at 60º simulated

using 92 measurements, b=1000s/mm^2, SNR=60, 6th order fitting with proper regularization gives lower angular error than the 4th order fitting (9° vs. 16°), higher success rate of resolving two fibers (1 vs. 0.998), but a lower ACC value (0.85 vs. 0.93) (complete comparison not shown).

As shown in figures 7 and 8, when data are analyzed through 4th order, measurements at $b = 2100s/mm^2$ produce lower angular deviation and higher ACC than at b values of 1000s/mm^2 or 3250s/mm^2. This result can be explained by the relationship between the coefficients $\vec{c}_l$ and the b value, and the relationship between the theoretical variance of $\vec{p}_{lm}$ and $\vec{c}_l$. According to Eq. [12], $\vec{c}_l$ depends on b value, $\lambda_\perp$ and the fitting order. Using the 4th order fitting $|c_l|$ reaches its maximum at $b = 2100s/mm^2$ for the value of $\lambda_\perp$ used in this study. The theoretical variance of $\vec{p}_{lm}$ is proportional to $1/|c_l|$ (see Appendix B for detailed derivation). Therefore, for a given $\lambda_\perp$ and 4th order fitting, b=2100s/mm^2 gives the smallest variance of $\vec{p}_{lm}$, which produces the most reliable FAD estimate.

The fact that the 92-direction acquisition outperforms the 32-direction acquisition confirms the hypothesis that the more measurements acquired, the higher the achievable angular resolution will be as a matter of practice. Since the acquisition time for HARD imaging is proportional to the number of diffusion directions, the time for one 92-direction scan roughly allows for three 32-direction scans. According to theory, the SNR of the averaged three 32-direction datasets should be about 1.7 times that of the one 92-direction data without averaging, i.e., the results from the 92-direction data at SNR

level of 20 should be comparable to the results from the 32-direction data at SNR level of 34. Our simulation results at $b=1000s/mm^2$ and SNR below 30 show close agreement with this theoretical prediction in terms of the angular deviation and ACC measures, as presented in figures 7 and 8. However, as the SNR increases, 92-direction measurement performs better than the imaging-time-matched 32-direction measurements. Furthermore, as the b value increases from $1000s/mm^2$ to $3250s/mm^2$, the advantage of the 92-measurement over the 32-measurement becomes more obvious, probably because the benefit of high diffusion sensitivity overrides the effect of the increased SNR. Another possible explanation is the non-linear relationships between the SNR and the evaluation figures of merit.

Discussion on the methods

A novel measure for performance evaluations, the ACC, was employed in this study. In earlier studies, figures of merit include angular error (23,44,54), volume fraction (44), the fiber crossing detection rate (54), root mean square error (55) and absolute error (56) between the noise-free diffusion profile and estimated diffusion profile, and the consistency fraction (a combination of the angular error and the fiber number estimation) (57). The ACC describes the similarity of the overall shape and orientation between two FADs. This measure contains more information about the FAD than any of the aforementioned measures alone. Therefore, performance evaluation based primarily on

ACC is more simple and reliable than using other figures of merit.

One factor affecting the conclusions of this study is the possible violation of the assumptions of the FORECAST model. The FORECAST model assumes that fibers are cylindrically symmetric and within each voxel all fiber components share same perpendicular diffusivity, which is not always true. Studies suggest that in some regions, the diffusion profile of a coherent fiber bundle may be oblate instead of cylindrical (38). An asymmetric fiber angular distribution within a voxel could also produce unequal perpendicular diffusivity. Violation of the identical perpendicular diffusivity assumption affects more the volume fraction than the fiber orientation estimation (28). In the two-fiber simulation of this study, in order to make the analysis simple, the perpendicular diffusivities and the volume fractions of the two fibers were set to be the same. Further investigation needs to be done in the future to explore how to make the estimation more reliable when these assumptions are violated.

Another factor affecting the conclusions of this study is the usage of the ACC relative to the ideal FAD as a performance measure. The ideal FAD may contain some small peaks around the origin which are considered artifacts due to truncation. As a result, an estimated FAD without false peaks may have a lower ACC score than a less perfect FAD with false peaks similar to the ideal one, which will certainly affect the accuracy of the performance evaluation. To address this problem, the estimate of the number of fibers and the total angular deviation within a voxel are considered in addition to the ACC value.

Finally, the weighting of each figure of merit for overall performance evaluation is arbitrary, resulting in approximately optimal ω. In order to minimize the effects of the individual analyzer and to reduce the processing time, future work is needed to develop an automatic algorithm for the choice of the optimal ω.

CHAPTER V

CONCLUSIONS

Using Monte Carlo simulations, this study examined the performance of the FORECAST model in terms of estimating intravoxel fiber structure using various imaging and analysis parameters. Based on the results of the simulation, the optimal imaging and processing parameters for conducting the FORECAST analysis can be determined, and the accuracy of the model can be estimated.

This study also shows a feasible method of even-order-fitting instead of the original full-fitting, to increase the fitting order and thus improve the angular resolution of the FORECAST model. The effect of this method on overall performance depends on the number of the diffusion measurements and the regularization method.

Another contribution of this study is the improvement of the FORECAST model by including Tikhonov regularization based on minimizing the non-physical negative FAD values. Both numerical simulation and *in vivo* human data analysis verified the improvements. The anisotropic smoothing algorithm also improves the angular accuracy of the fiber orientation estimation as demonstrated in the *in vivo* human data.

With the techniques listed above, the FORECAST model becomes more robust to noise. More reliable estimates of the fiber orientation and fiber coherence will be useful

in studies aimed at fiber tractography and white matter disease detection.

THIRTY-TWO DIFFUSION DIRECTIONS

Table 2. List of the Cartesian coordinates of the 32 unit vectors uniformly distributed over a sphere used by the Philips scanner system.

x	y	z	x	y	z
1	0	0	0.7771	0.4707	-0.4178
0	1	0	0.9242	-0.1036	-0.3677
0	0	1	0.4685	-0.7674	-0.4378
-0.0424	-0.1146	-0.9925	0.8817	-0.1893	-0.4322
0.1749	-0.2005	-0.9639	0.6904	0.7062	-0.1569
0.2323	-0.1626	-0.959	0.2391	0.7571	-0.608
0.3675	0.0261	-0.9296	-0.0578	0.9837	0.1703
0.1902	0.3744	-0.9076	-0.5368	0.8361	-0.1135
-0.1168	0.8334	-0.5402	-0.9918	-0.1207	-0.0423
-0.2005	0.2527	-0.9466	-0.9968	0.0709	-0.0379
-0.4958	0.1345	-0.858	-0.8724	0.4781	-0.1014
-0.0141	-0.6281	-0.778	-0.2487	0.9335	0.2581
-0.7445	-0.1477	-0.6511	0.1183	0.9919	-0.0471
-0.7609	0.3204	-0.5643	0.3376	0.8415	0.4218
-0.1809	0.9247	-0.3351	0.5286	0.8409	0.1163
-0.6796	-0.4224	-0.5997	0.9969	0.055	-0.0571

APPENDIX B

THEORETICAL PREDICTION OF THE VARIANCE OF p_{lm}

According to Eq. [11],

$$p_{lm} = \frac{s_{lm}}{s_0 c_l} \qquad [20]$$

For given b value, mean diffusivity $\overline{\lambda}$, and perpendicular diffusivity $\lambda_{\perp}$, c_l is determined according to Eq. [12]. Therefore,

$$
\begin{aligned}
\sigma_{p_{lm}}^2 &= \left(\frac{\partial p_{lm}}{\partial s_{lm}}\right)^2 \sigma_{s_{lm}}^2 + \left(\frac{\partial p_{lm}}{\partial s_0}\right)^2 \sigma_{s_0}^2 \\
&= \left(\frac{1}{c_l s_0}\right)^2 \sigma_{s_{lm}}^2 + \left(-\frac{s_{lm}}{c_l s_0^2}\right)^2 \sigma_{s_0}^2 \\
&= \left(\frac{\sigma_{s_{lm}}}{c_l s_0}\right)^2 + \left(-\frac{p_{lm}}{s_0}\right)^2 \sigma_{s_0}^2 \\
&= \left(\frac{s_{lm}}{c_l s_0}\right)^2 \frac{\sigma_{s_{lm}}^2}{s_{lm}^2} + p_{lm}^2 \frac{\sigma_{s_0}^2}{s_0^2} \\
&= p_{lm}^2 \cdot \left(\frac{\sigma_{s_{lm}}^2}{s_{lm}^2} + \frac{\sigma_{s_0}^2}{s_0^2}\right) \\
&= p_{lm}^2 \frac{\sigma_{s_0}^2}{s_0^2}\left(1 + \frac{\sigma_{s_{lm}}^2}{\sigma_{s_0}^2} \cdot \frac{s_0^2}{s_{lm}^2}\right)
\end{aligned}
\qquad [21]
$$

According to Eq. [6], the variance of s_{lm} is

$$\sigma_{s_{lm}}^2 = \sigma_s^2 \left(\tilde{X}'\tilde{X}\right)_{kk}^{-1} \qquad [22]$$

where σ_s^2 is the variance of the diffusion-weighted signal, $\left(\tilde{X}'\tilde{X}\right)_{kk}^{-1}$ is the kth element on

the diagonal of the matrix $\left(\tilde{X}'\tilde{X}\right)^{-1}$, $k = l^2 + l + m + 1$. Assuming the variance of the diffusion-weighted signal σ_s^2 equals the variance of the non-diffusion weighted signal $\sigma_{s_0}^2$, Eq. [22] becomes

$$\sigma_{s_{lm}}^2 = \sigma_{s_0}^2 \left(\tilde{X}'\tilde{X}\right)_{kk}^{-1} \tag{23}$$

Inserting Eq. [23] into Eq. [21], we have

$$\begin{aligned}
\sigma_{p_{lm}}^2 &= p_{lm}^2 \frac{\sigma_{s_0}^2}{s_0^2} \left(1 + \left(\tilde{X}'\tilde{X}\right)_{kk}^{-1} \cdot \frac{s_0^2}{s_{lm}^2} \right) \\
&= \frac{1}{SNR^2} \left(p_{lm}^2 + \left(\tilde{X}'\tilde{X}\right)_{kk}^{-1} \frac{1}{c_l^2} \right)
\end{aligned} \tag{24}$$

Therefore, for a given fitting order l, to minimize the variance of p_{lm}, a proper b value should be chosen to maximize the $|c_l|$.
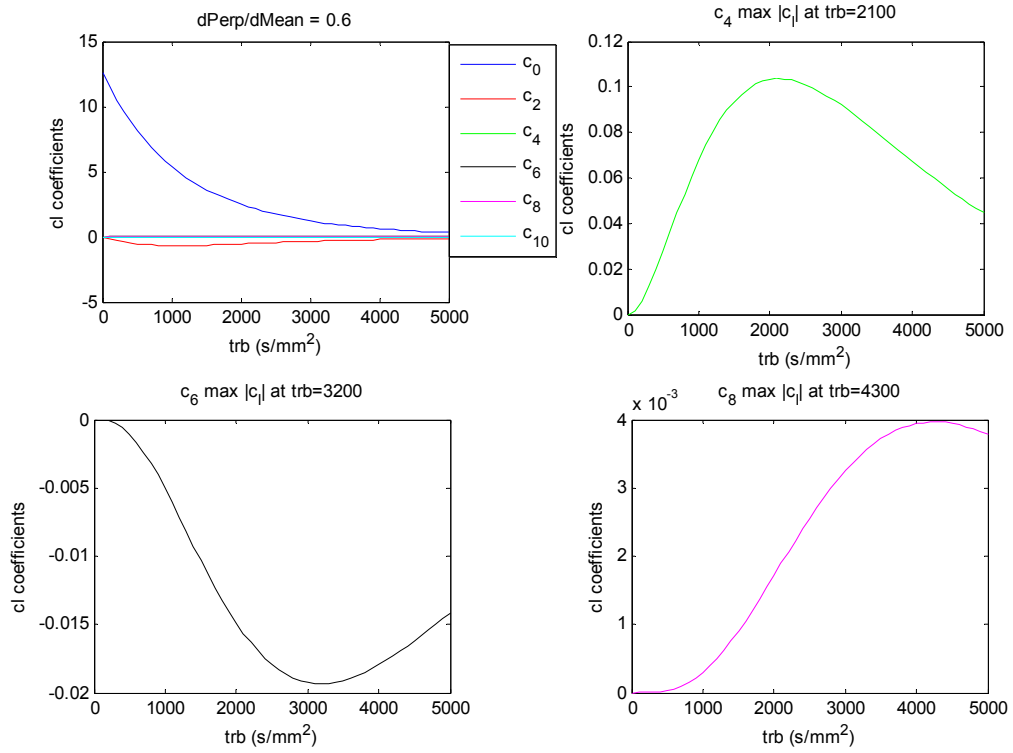
Figure 14. Coefficients c_l vs. $tr(\tilde{b})$. Subplot in top left shows c_l for even orders from 0 to 10. The other subplots show c_l for orders 4, 6 and 8.

REFERENCES

1.   Basser PJ, Mattiello J, LeBihan D. MR diffusion tensor spectroscopy and imaging. Biophysical journal 1994;66(1):259-267.

2.   Basser PJ, Pierpaoli C. Microstructural and physiological features of tissues elucidated by quantitative-diffusion-tensor MRI. Journal of magnetic resonance 1996;111(3):209-219.

3.   Beaulieu C. The basis of anisotropic water diffusion in the nervous system - a technical review. NMR in biomedicine 2002;15(7-8):435-455.

4.   Conturo TE, Lori NF, Cull TS, Akbudak E, Snyder AZ, Shimony JS, McKinstry RC, Burton H, Raichle ME. Tracking neuronal fiber pathways in the living human brain. Proceedings of the National Academy of Sciences of the United States of America 1999;96(18):10422-10427.

5.   Mori S, Wakana S, Nagae-Poetscher LM, van Zijl PCM. MRI atlas of human white matter. Amsterdam: Elsevier; 2005.

6.   Mori S, Crain BJ, Chacko VP, van Zijl PC. Three-dimensional tracking of axonal projections in the brain by magnetic resonance imaging. Annals of neurology 1999;45(2):265-269.

7.   Miller SP, Vigneron DB, Henry RG, Bohland MA, Ceppi-Cozzio C, Hoffman C, Newton N, Partridge JC, Ferriero DM, Barkovich AJ. Serial quantitative diffusion tensor MRI of the premature brain: development in newborns with and without injury. J Magn Reson Imaging 2002;16(6):621-632.

8.   Warach S, Chien D, Li W, Ronthal M, Edelman RR. Fast magnetic resonance diffusion-weighted imaging of acute human stroke. Neurology 1992;42(9):1717-1723.

9.   Miller DH, Grossman RI, Reingold SC, McFarland HF. The role of magnetic resonance techniques in understanding and managing multiple sclerosis. Brain 1998;121 (Pt 1):3-24.

10.   Hugg JW, Butterworth EJ, Kuzniecky RI. Diffusion mapping applied to mesial

temporal lobe epilepsy: preliminary observations. Neurology 1999;53(1):173-176.

11.   Ito R, Melhem ER, Mori S, Eichler FS, Raymond GV, Moser HW. Diffusion tensor brain MR imaging in X-linked cerebral adrenoleukodystrophy. Neurology 2001;56(4):544-547.

12.   Kono K, Inoue Y, Nakayama K, Shakudo M, Morino M, Ohata K, Wakasa K, Yamada R. The role of diffusion-weighted imaging in patients with brain tumors. Ajnr 2001;22(6):1081-1088.

13.   Nusbaum AO, Tang CY, Buchsbaum MS, Wei TC, Atlas SW. Regional and global changes in cerebral diffusion with normal aging. Ajnr 2001;22(1):136-142.

14.   Ricci PE, Burdette JH, Elster AD, Reboussin DM. A comparison of fast spin-echo, fluid-attenuated inversion-recovery, and diffusion-weighted MR imaging in the first 10 days after cerebral infarction. Ajnr 1999;20(8):1535-1542.

15.   Sorensen AG, Wu O, Copen WA, Davis TL, Gonzalez RG, Koroshetz WJ, Reese TG, Rosen BR, Wedeen VJ, Weisskoff RM. Human acute cerebral ischemia: detection of changes in water diffusion anisotropy by using MR imaging. Radiology 1999;212(3):785-792.

16.   Tievsky AL, Ptak T, Farkas J. Investigation of apparent diffusion coefficient and diffusion tensor anisotrophy in acute and chronic multiple sclerosis lesions. Ajnr 1999;20(8):1491-1499.

17.   Bozzali M, Cercignani M, Sormani MP, Comi G, Filippi M. Quantification of brain gray matter damage in different MS phenotypes by use of diffusion tensor MR imaging. Ajnr 2002;23(6):985-988.

18.   Cercignani M, Bozzali M, Iannucci G, Comi G, Filippi M. Intra-voxel and inter-voxel coherence in patients with multiple sclerosis assessed using diffusion tensor MRI. Journal of neurology 2002;249(7):875-883.

19.   Eriksson SH, Rugg-Gunn FJ, Symms MR, Barker GJ, Duncan JS. Diffusion tensor imaging in patients with epilepsy and malformations of cortical development. Brain 2001;124(Pt 3):617-626.

20.   Krabbe K, Gideon P, Wagn P, Hansen U, Thomsen C, Madsen F. MR diffusion imaging of human intracranial tumours. Neuroradiology 1997;39(7):483-489.

21. Guo AC, Cummings TJ, Dash RC, Provenzale JM. Lymphomas and high-grade astrocytomas: comparison of water diffusibility and histologic characteristics. Radiology 2002;224(1):177-183.

22. Wiegell MR, Larsson HB, Wedeen VJ. Fiber crossing in human brain depicted with diffusion tensor MR imaging. Radiology 2000;217(3):897-903.

23. Tuch DS, Reese TG, Wiegell MR, Makris N, Belliveau JW, Wedeen VJ. High angular resolution diffusion imaging reveals intravoxel white matter fiber heterogeneity. Magn Reson Med 2002;48(4):577-582.

24. Alexander DC, Barker GJ, Arridge SR. Detection and modeling of non-Gaussian apparent diffusion coefficient profiles in human brain data. Magn Reson Med 2002;48(2):331-340.

25. Frank LR. Anisotropy in high angular resolution diffusion-weighted MRI. Magn Reson Med 2001;45(6):935-939.

26. Ozarslan E, Mareci TH. Generalized diffusion tensor imaging and analytical relationships between diffusion tensor imaging and high angular resolution diffusion imaging. Magn Reson Med 2003;50(5):955-965.

27. Jansons KM, Alexander DC. Persistent Angular Structure: new insights from diffusion MRI data. Dummy version. Inf Process Med Imaging 2003;18:672-683.

28. Anderson AW. Measurement of fiber orientation distributions using high angular resolution diffusion imaging. Magn Reson Med 2005;54(5):1194-1206.

29. Moseley ME, Cohen Y, Kucharczyk J, Mintorovitch J, Asgari HS, Wendland MF, Tsuruda J, Norman D. Diffusion-weighted MR imaging of anisotropic water diffusion in cat central nervous system. Radiology 1990;176(2):439-445.

30. Pierpaoli C, Basser PJ. Toward a quantitative assessment of diffusion anisotropy. Magn Reson Med 1996;36(6):893-906.

31. Basser PJ, Mattiello J, LeBihan D. Estimation of the effective self-diffusion tensor from the NMR spin echo. Journal of magnetic resonance 1994;103(3):247-254.

32. Stejskal EO, Tanner JE. Spin diffusion measurements: spin echoes in the presence of a time-dependent field gradient. J Chem Phys 1965;42:288-292.

33. Mori S, van Zijl PC. Fiber tracking: principles and strategies - a technical review. NMR in biomedicine 2002;15(7-8):468-480.

34. Lori NF, Akbudak E, Shimony JS, Cull TS, Snyder AZ, Guillory RK, Conturo TE. Diffusion tensor fiber tracking of human brain connectivity: aquisition methods, reliability analysis and biological results. NMR in biomedicine 2002;15(7-8):494-515.

35. Khong PL, Leung LH, Fung AS, Fong DY, Qiu D, Kwong DL, Ooi GC, McAlanon G, Cao G, Chan GC. White matter anisotropy in post-treatment childhood cancer survivors: preliminary evidence of association with neurocognitive function. J Clin Oncol 2006;24(6):884-890.

36. Hall DE, Moffat BA, Stojanovska J, Johnson TD, Li Z, Hamstra DA, Rehemtulla A, Chenevert TL, Carter J, Pietronigro D, Ross BD. Therapeutic efficacy of DTI-015 using diffusion magnetic resonance imaging as an early surrogate marker. Clin Cancer Res 2004;10(23):7852-7859.

37. Dong Q, Welsh RC, Chenevert TL, Carlos RC, Maly-Sundgren P, Gomez-Hassan DM, Mukherji SK. Clinical applications of diffusion tensor imaging. J Magn Reson Imaging 2004;19(1):6-18.

38. Alexander AL, Hasan KM, Lazar M, Tsuruda JS, Parker DL. Analysis of partial volume effects in diffusion-tensor MRI. Magn Reson Med 2001;45(5):770-780.

39. Poupon C, Bloch I. Détection des faisceaux de fibres de la substance blanche pour l'étude de la connectivité anatomique cérébrale (Tracking of white matter fiber bundles for the study of cerebral connectivity). Paris, FRANCE: Ecole nationale supérieure des télécommunications; 1999.

40. Pierpaoli C, Barnett A, Pajevic S, Chen R, Penix LR, Virta A, Basser P. Water diffusion changes in Wallerian degeneration and their dependence on white matter architecture. NeuroImage 2001;13(6 Pt 1):1174-1185.

41. Tuch DS. MRI of complex tissue structure. Cambridge, Massachusetts: Harvard University-Massachusetts Institute of Technology; 2002.

42. Liu C, Bammer R, Acar B, Moseley ME. Characterizing non-Gaussian diffusion by using generalized diffusion tensors. Magn Reson Med 2004;51(5):924-937.

43. Frank LR. Characterization of anisotropy in high angular resolution

diffusion-weighted MRI. Magn Reson Med 2002;47(6):1083-1099.

44. Tournier JD, Calamante F, Gadian DG, Connelly A. Direct estimation of the fiber orientation density function from diffusion-weighted MRI data using spherical deconvolution. NeuroImage 2004;23(3):1176-1185.

45. Zhan W, Stein EA, Yang Y. Mapping the orientation of intravoxel crossing fibers based on the phase information of diffusion circular spectrum. NeuroImage 2004;23(4):1358-1369.

46. Tuch DS, Reese TG, Wiegell MR, Wedeen VJ. Diffusion MRI of complex neural architecture. Neuron 2003;40(5):885-895.

47. Tuch DS. Q-ball imaging. Magn Reson Med 2004;52(6):1358-1372.

48. Wedeen VJ, Reese TG, Tuch DS, Weigel MR, Dou J-G, Weiskoff RM, Chessler D. Mapping fiber orientation spectra in cerebral white matter with Fourier-transform diffusion MRI. Proc Intl Soc Mag Reson Med 2000;8:82.

49. Hong X, Anderson AW, Ding Z. Resolve Fiber Orientation Ambiguity Using HARD Imaging. Proc Intl Soc Mag Reson Med 2006;14:2728.

50. Zwillinger D. Handbook of Differential Equations. Boston, MA: Academic Press; 1997.

51. Hansen PC. Regularization Tools: A Matlab Package For Analysis and Solution of Discrete Ill-posed Problems. Numerical algorithms 1994;6:1-35.

52. Tournier JD, Calamante F, Connelly A. Improved characterisation of crossing fibres: spherical deconvolution combined with Tikhonov regularization. Proc Intl Soc Mag Reson Med 2006;14:645.

53. Ding Z, Gore JC, Anderson AW. Reduction of noise in diffusion tensor images using anisotropic smoothing. Magn Reson Med 2005;53(2):485-490.

54. Kreher BW, Schneider JF, Mader I, Martin E, Hennig J, Il'yasov KA. Multitensor approach for analysis and tracking of complex fiber configurations. Magn Reson Med 2005;54(5):1216-1225.

55. Hess CP, Mukherjee P, Han ET, Xu D, Vigneron DB. Q-ball reconstruction of multimodal fiber orientations using the spherical harmonic basis. Magn Reson

Med 2006;56(1):104-117.

56.   Descoteaux M, Angelino E, Fitzgibbons S, Deriche R. Apparent diffusion coefficients from high angular resolution diffusion imaging: estimation and applications. Magn Reson Med 2006;56(2):395-410.

57.   Alexander DC. Multiple-fiber reconstruction algorithms for diffusion MRI. Annals of the New York Academy of Sciences 2005;1064:113-133.